UNIVERSITÀ DEGLI STUDI DI ROMA
“TOR VERGATA”

Facoltà di Ingegneria

Corso di Laurea in Ingegneria Meccanica

Tesi di Laurea Magistrale in Ingegneria Meccanica

Structural Design and Optimization of the Wind Tunnel model of the EU RIBES Project.

Thesis supervisor

Eng. Marco Evangelos Biancolini

Candidate

Marco Fontanella

Assistant supervisors

PhD Eng. Corrado Groth

Eng Ubaldo Cella

Anno Accademico 2012/2013

Dire che la scienza è logica è come

dire che la pittura è dipinta.

Leon Cooper

Chapter 1 Introduction

The present work is part of the european RIBES Project. The goal of RIBES Project (**R**adial basis function at fluid **I**nterface **B**oundaries to **E**nvelope flow results for advanced **S**tructural analysis) is to achieve an overall improvement of aircraft performances by means of a correct and efficient load mapping between FEM and CFD softwares. The project is mainly divided in two parts: the software development and the WT validation of its results.

In this work the WT model will be designed and optimized. The wind tunnel experimentation on this model will provide a reliable data sheet so that software's results will be confronted and validated with such datas.

The structural part of the analysis will be performed, while the aerodynamic one has been previously completed.

In Chapter 2 the RIBES project will be deeply presented and the geometry of the model will be described.

In Chapter 3 a general overview of the theory of airfoils will be given introducing the physical phenomena, parameters and governing equations typical of this type of applications. The description of structural elements and their behavior is also given, as well as an explanation of the way they transfer loads between each other.

In Chapter 4 are presented the steps done to have a working FEM model ready to be analyzed (mean surfaces extraction, mesh features, load transfer). The wind tunnel test will be shortly presented. In this chapter there will also be the description of the analysis tools provided by FEMAP.

In Chapter 5 the results of the analysis performed are described and commented. FEMAP's modal, static, buckling and optimization routines are run so that the model is designed accordingly. The validation of these results are performed by means of the beam and thin plates theories. The characteristic of the DOE campaign are also described.

In Chapter 6 the conclusions of this work are summarized and future works related to this thesis are briefly discussed.

Chapter 2 RIBES Project

Project Overview

With the passing years, care and preservation of the environment is becoming of greater importance in every engineering field. One of the cause of pollution and changes in chemical air composition is the transportation sector, whose emissions (mainly CO_2 and NO_x) are responsible of the greenhouse effect.

The reduction of polluting output can be achieved in several ways:

- Installation of pollution abatement systems, which, in general, leads to a worsening of overall efficiency (as for automobile's catalytic converters);
- The use of finer, and therefore more expensive, fuels;
- Pre-engineering and optimization of the whole system.

This is the context where the EU project Clean Sky 2 is situated. Its main goal is to define an overall optimization strategy in order to mitigate Europe's aircraft fleet ambient impact. Clean Sky's environmental objectives can be considered achieved only when the demonstrators are run and the maturity of the technologies is confirmed. In the meantime, the technologies are selected and tested, allowing an increasingly precise forecast of the expected results. The goals of the program can be resumed in the following list compared to corresponding 2000 data:

- 50% reduction in CO_2 emissions per ton-km;
- 80% reduction in NO_x emissions per ton-km;
- 50% reduction in perceived noise;
- A substantial improvement in the aircraft lifecycle impact on the environment.

RIBES Objectives

The core of Clean Ky2 is the mandatory requirement to mitigate pollutant emissions and fuel consumption by means of a generalized optimization process that must regard not only the shape and the materials employed, as usual in the past decades, but also through the availability of efficient design tools that can allow to reduce the weight, to optimize configurations and therefore to increase the performances of aircrafts. The goal of reducing the weight can be obtained if reliable numerical methodologies will be studied and implemented in order to simulate fluid dynamic loads between numerical models, to guarantee a safer design optimization workflow that allows a reduction of uncertainties, gaining the goal of weight reduction. This problem poses a technological challenge especially for numerical models of complex aerospace structures there flow data exchange between not matching CFD and FEM meshes has to be performed on huge calculation models (several millions cells).

The research project proposes an innovative approach for loads mapping based on Radial Basis Functions (RBF) theory and RIBES software implementation. A technology previously developed in the field of mesh morphing (RBF Morph) capable to deal with large dataset will be used to enable an accurate mapping. The effectiveness of the approach will be demonstrated on an aeronautic wing structure by means of numerical and experimental checks and by a quantitative estimation of weight reduction obtained using the optimization module included in the RIBES application.

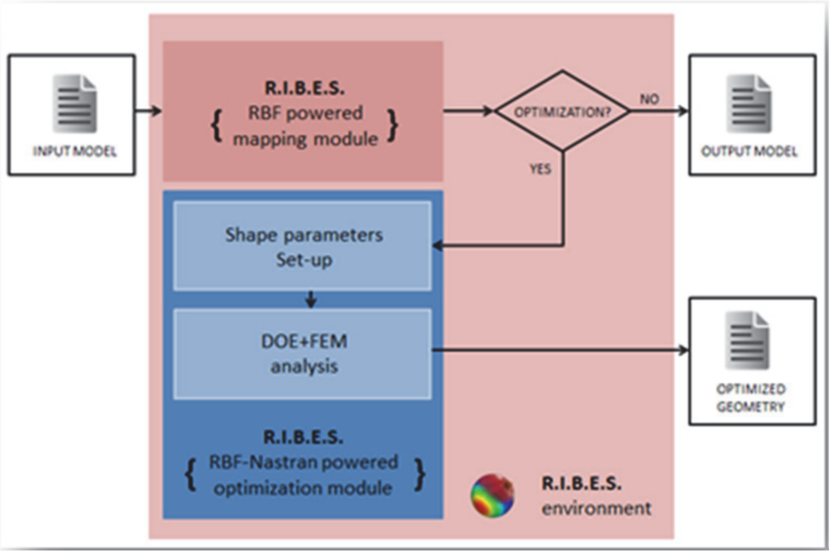

Figure 1

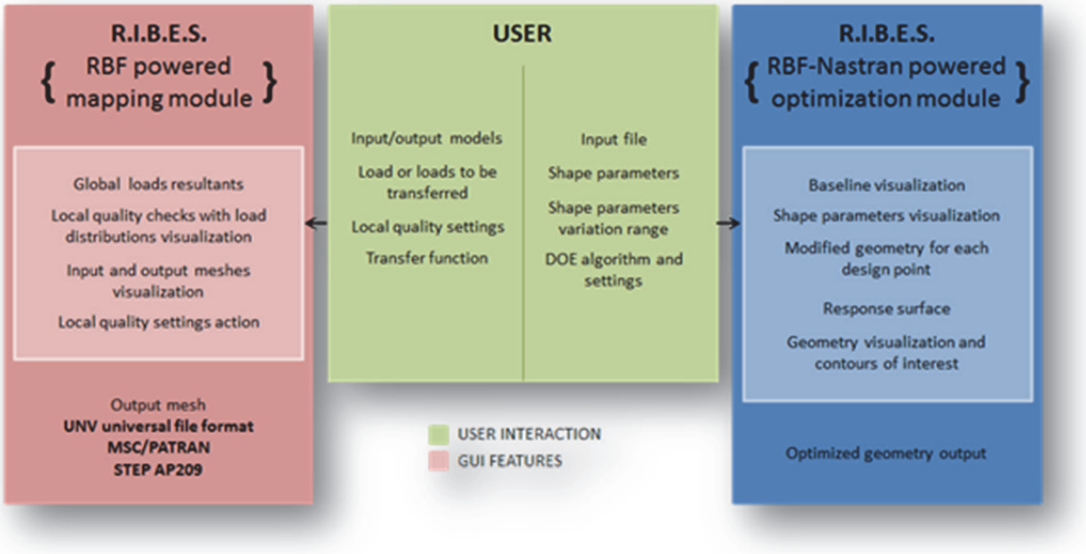

Figure 2

In this work, the structural analysis of the wind tunnel model is performed. A deep and continuous data exchange between wing's CFD and FEM models is needed in order for the analysis to be successful.

Wind Tunnel model

The accuracy of the developed load transfer numerical tools, will be validated against a case of aeronautical interest. Such a test case should accomplish the task of being significant of a realistic design problem and being suitable to be experimentally verified.

A typical wing structure will be developed referring to a realistic aircraft. In order to maximize the interaction between aerodynamic loads and wing deformation, a swept back wing will be adopted. Furthermore, to maximize the load similitude with a scaled wing structure model to be experimentally verified in a low speed wind tunnel, a relatively low wing load case should be selected. With this vision, the wing is supposed to refer to a geometry suitable for an ultra-light jet class aircraft.

Table 1

Aircraft Configuration	
Wing Span	9.5 m
Reference wing surface	12 m^2
MTOW	2160 Kg
Service ceiling	41000 ft (12500 m)
Cruise Mach	0.75

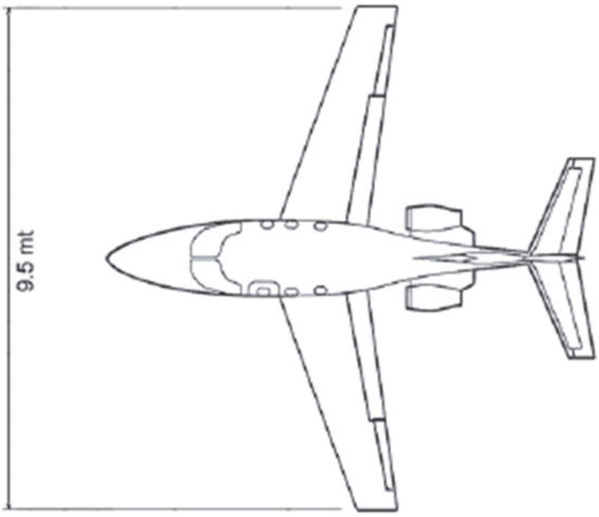

Figure 3 Aircraft Configuration

The objective of the wind tunnel test will be to provide a database of experimental measurements, in terms of loads, stresses and displacements to be compared with the analysis performed, in the same conditions, by a numerical aeroelastic analysis environment. Such tool integrates the FEM model of the wing structure and the CFD computation coupled by the load mapping and transferring tool developed within the project. At this aim a scaled wind tunnel model of the exposed part of half wing in clean configuration, reproducing a typical wing box structure, will be built.

A complete structural and load similitude at testing conditions would require a relatively high speed which is not compatible with a typical not pressurized low speed wind tunnel with a sufficient large test section (the speed required to generate a similar scaled load on a model with a span smaller than 2 meter, assuming the same full scale aircraft wing load and design cruising lift coefficient, would be higher than Mach 0.3). Such task, in any case, is not the objective of the experimental tests. It is then assumed to orient the setup of the test campaign to the conservation of the similitude in terms of amount of model deformation and shape of wing load distribution. This configuration will provide an efficient base of validation representative of a typical design case.

The scale model, to be used for the validation, will be 1:2.5 to which corresponds a span of 1.6 meters. Figure 4 details its dimensions

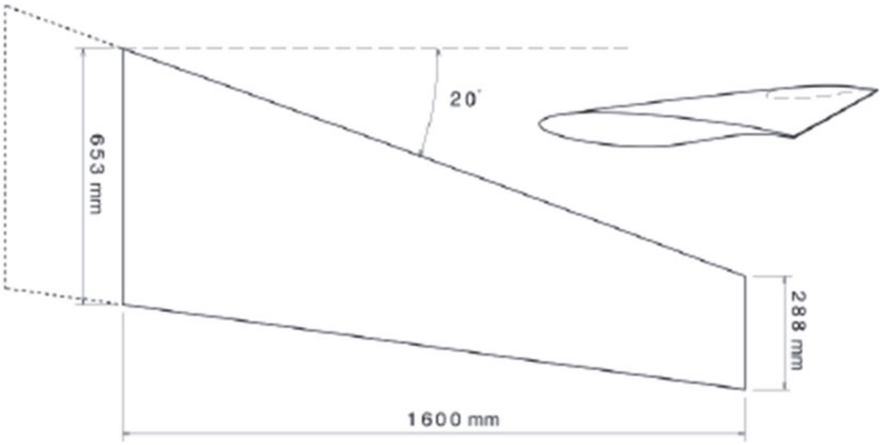

Figure 4 Wing Tunnel model geometry

Table 2

Wind tunnel model geometry	
Model scale	1:2.5
Span	1600 mm
Reference Surface	0.754 m^2
MAC	495 mm
Root chord	653 mm
Tip chord	288 mm
Root thickness	85 mm

Tip thickness	29 mm
LE sweep angle	20°

A number of 80 pressure taps will be installed on both pressure and suction side of the model along the span and along to sections at two stations in order to provide a reasonable crowded cloud of point to be compared to the CFD distribution estimation.

A marker matrix will be placed on the surface model and a photogrammetry technique will be adopted to evaluate the structural deformation. The geometric displacement will be reconstructed in 3D and compared to the FEM computed deformation.

The test matrix will cover a speed range from 35 to 45 m/s. Several wing polars will be measured and the wing deformation at the most significant test conditions will be reconstructed from the recorded images.

The fluid dynamic computational domain will reproduce the wind tunnel configuration.

The structural numerical model will be coupled to the CFD code in an FSI computational environment and the most significant points of the WT test matrix will be reproduced and compared to the measurements.

Chapter 3 Theory of Airfoils and layout of wing’s structure

Description of the geometry

An airfoil is an ideal, plane figure which represents the transverse section of a wing.

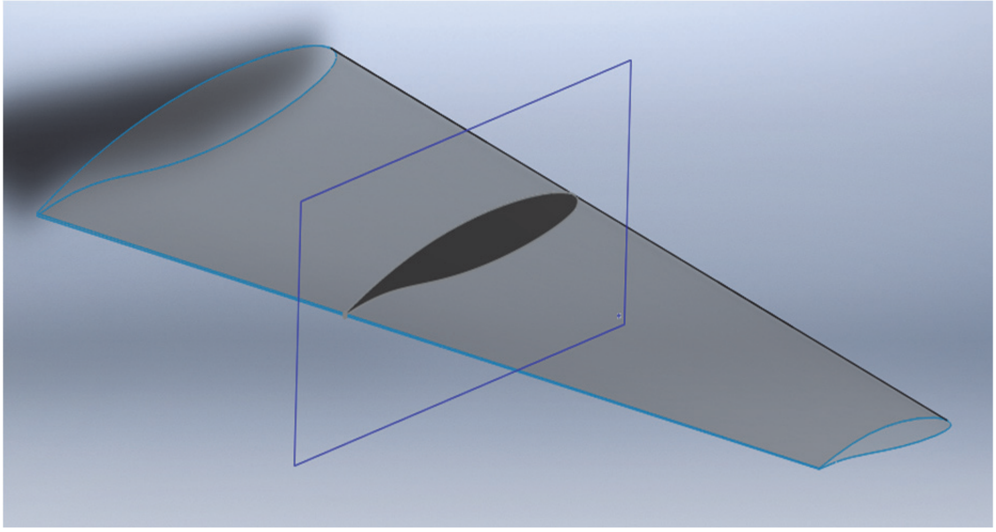

Figure 5 Airfoil

The geometry of this profile is fully described using two informations:

- The law of the mean line,
- The distribution of thickness perpendicular to the mean line.

The superior part of the profile is the *upper contour*, the inferior one is the *lower contour*.

The profile is symmetric if characterized by a straight mean line, otherwise it is convex.

The airfoil is surrounded by a plane flow described by:

- *Undisturbed flow speed* V or U_∞,
- *Undisturbed density* ρ_∞,
- *Undisturbed pressure* p_∞.

Other typical elements of airfoils are:

- **Angle of attack α:** angle between chord line and undisturbed flow,
- **Leading edge LE:** point corresponding to the front of the mean line (2),
- **Trailing edge TE:** point corresponding to the back of the mean line (7),
- **Osculatory circle of the LE:** (3),
- **Chord line c:** segment joining leading and trailing edges,
- **Curvature:** (4),
- **Upper contour:** (6),
- **Lower contour:** (7),
- **Thickness:** Distance between upper and lower contours (5),
- **Mean line:** (8),
- **Line of zero lift:** line, passing through the TE, parallel to the flow speed producing no lift (1),
- **Wingspan b:** the distance between wingroot (where the wing joins the fuselage) and wingtip (the biggest distance from the fuselage),
- **Aspect ratio A:** ratio of wingspan and mean chord,
- **Taper ratio λ:** ratio of chord tip and chord root.

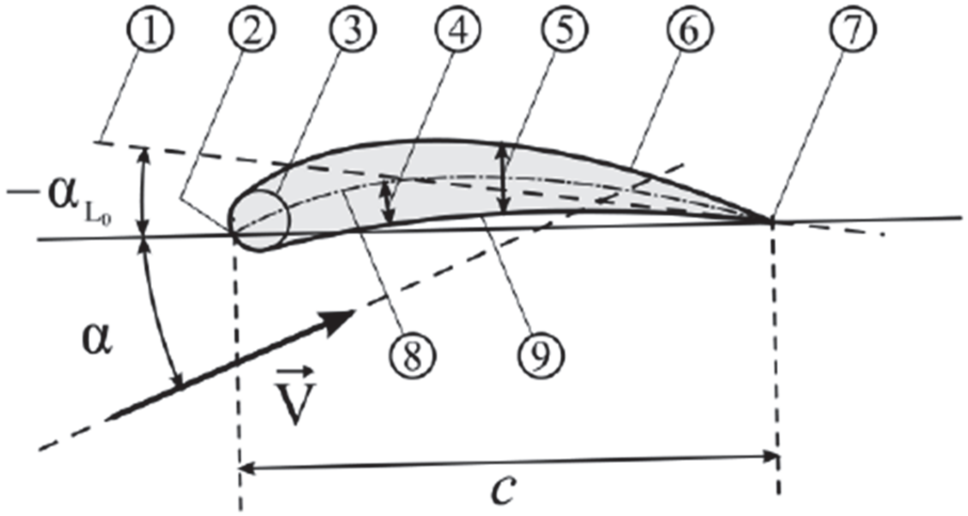

Figure 6 Airfoils' geometric parameters

The wing box analyzed in the present work is essentially a bended laminate. Due to this, when referring to thickness one mean the thickness of the laminate itself.

Flight dynamics and physics

An airfoil-shaped body moving through a fluid produces an aerodynamic force. The component of this force perpendicular to the direction of motion is called lift. component parallel to the direction of motion is called drag. Subsonic flight airfoils have a characteristic shape with a rounded leading edge, followed by a sharp trailing edge, often with asymmetric camber. The lift on an airfoil is primarily the result of its angle of attack, shape and flight conditions.

The total force F generated on an airfoil has two main contributes: one depending on the pressure and another one depending on the shear viscous stresses.

$$\bar{F} = \int (-p\hat{n} + \tau\hat{t})dS$$

Where $\hat{n}$ and $\hat{t}$ are the unit vectors normal and tangential to the aircraft surface.

Another way to express F is:

$$F = \frac{1}{2}\rho V^2 S c_f$$

And it can be represented by three components among the axes (x_B, y_B, z_B):

$$F = -\begin{bmatrix} D \\ S \\ L \end{bmatrix} = -\frac{1}{2}\rho V^2 S \begin{bmatrix} C_D \\ C_S \\ C_L \end{bmatrix}$$

Where ρ is the density of the fluid, S the cross-sectional area, V is the speed modulus of the object relative to the fluid and C_f is a vector which components are the aerodynamic coefficients. These coefficients are C_D, C_L and C_S and they depend on the speed, Reynolds number and Mach number. Both lift (L) and drag (D) have a large effect on performances of the plane. The aerodynamic resistance is parallel and opposite to the free-stream direction V and it is mainly a dissipative force so the aircraft needs a forward thrust sistem to fly. The lift is perpendicular to the flow direction so it doesn’t do any work.

Types of drag are generally divided into the following categories:

- Parasitic drag, consisting of
  - Form drag,
  - Skin friction,
  - Interference drag,
- Lift-induced drag
- Wave drag

The term parasitic drag is mainly used in aerodynamics, since for lifting wings drag is in general smaller than lift. Considering flows around bluff bodies, drag is most often dominating, and then the qualifier “parasitic” is meaningless. Form drag, skin friction and interference drag on bluff bodies are not counted as being elements of "parasitic drag", but directly as elements of drag. Further, lift-induced drag is only relevant when wings or a lifting body are present, and it is therefore usually discussed either in the aviation perspective of drag, or in the design of either semi-planing or planing hulls. Wave drag occurs when a solid object is moving through a fluid at or near the speed of sound.

Aerodynamic coefficients

Once the aerodynamic forces are defined it is possible to characterize the relative coefficients:

$$C_L = \frac{L}{\frac{1}{2}\rho_\infty V_\infty^2 S},$$

$$C_D = \frac{D}{\frac{1}{2}\rho_\infty V_\infty^2 S},$$

$$C_M = \frac{M}{\frac{1}{2}\rho_\infty V_\infty^2 S c},$$

These parameters are very useful to evaluate the airplane efficiency and to determine the finest configuration. It is common to show, for a particular airfoil section, the relationship between section lift coefficient and angle of attack:

$$C_L = C_{L\alpha}(\alpha - \alpha_0)$$

If the airfoil is enough thin, $C_{L\alpha} \approx 2\pi$ and it doesn't depend on the airfoil camber and thickness; α_0 is the angle of attack corresponding to the zero lift condition. The lift coefficient is strictly affected by several factors: C_L= f(α,Re,Ma,shape). The angle at which maximum lift coefficiet occurs is the stall angle, over this value the lift coefficient decreases as shown in Figure 7

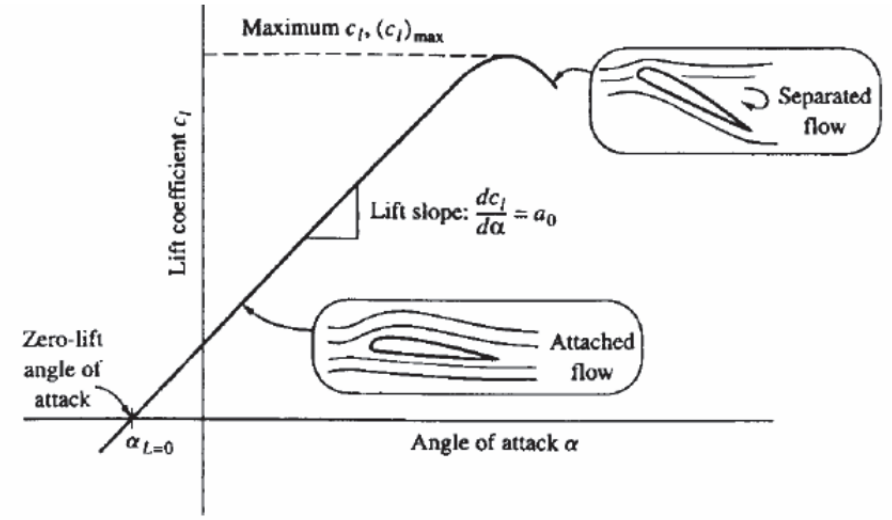

Figure 7 C_L vs Angle of Attack

The next Figure shows a typical non-linear plot of C_D vs α. Other affecting coefficients are C_D= f(α,Re,Ma,shape).

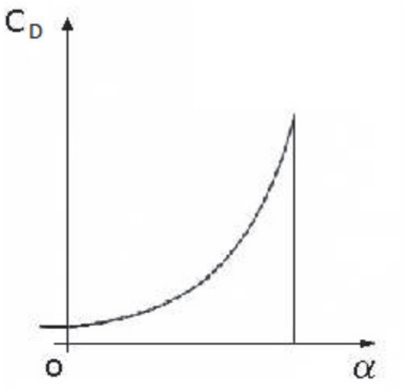

Figure 8 C_D vs Angle of Attack

The relationship between lift and drag is the *efficiency* and it is also called lift-to-drag ratio and it is represented by the polar plot:

$$E = \frac{C_L}{C_D}$$

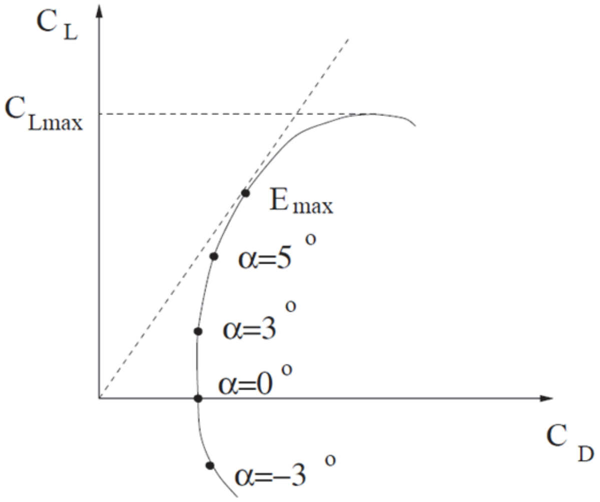

Figure 9 Efficiency (Polar)

Efficiency is useful to choose the best aifoil, it is possible to find its maximum value drawing a tangent line to the polar drag passing through the origin.

Pressure coefficient is another important coefficient in aerodynamics which describes the relative pressures throughout a flow field.

$$C_P(x) = \frac{p(x) - p_\infty}{\frac{1}{2}\rho V_\infty^2}$$

In the fluid flow field around a body there will be points having positive pressure coefficients up to one, and negative pressure coefficients including coefficients less than minus one, but nowhere will the coefficient exceed plus one because the highest pressure that can be achieved is the stagnation pressure (there can be exceptions for compressible flows).

On the upper surface of the airfoil the pressure is less than the freestream pressure $p<p_\infty$ so the $C_p<0$, whereas in the lower surface $p>p_\infty$ and $C_p>0$. The point P is the stagnation point where the pressure is the stagnation pressure, the speed is equal to zero and $C_p=1$.

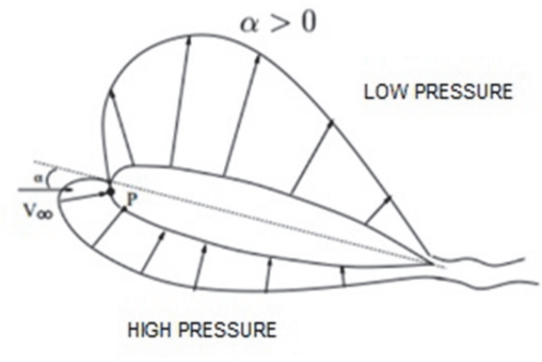

Figure 10 Pressure distribution

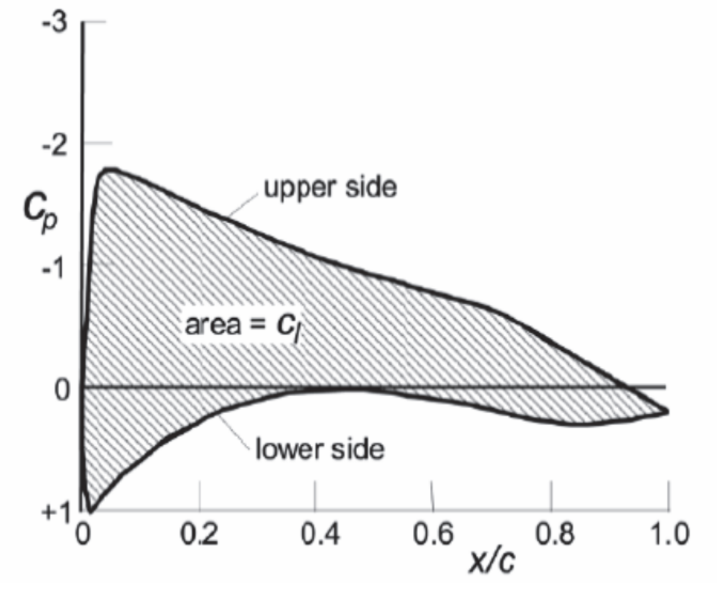

Figure 11 C_p along the spanwise direction

A tipical coefficient pressure distribution on an airfoil is shown in Figure 10. The coefficient of lift for an airfoil can be calculated from the coefficient of pressure distribution calculating the area between the lines on the distribution.

Figure 12 shows different rotational motions exhibited by an aircraft. Pitching moment is expressed about the center of gravity of the aircraft (always situated where the leading edges connect with the fuselage).

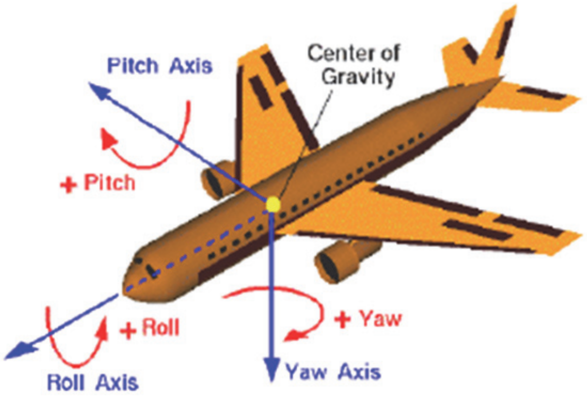

Figure 12 Pitch, Yaw and Roll motions of an Aircraft

Layout of wing structure.

A real commercial aircraft wing contains thousands of structural components. Creation of a detailed wing model by simultaneously incorporating all the wing features is virtually impossible. Thus, engineers rely on simplified models that provide a fairly accurate approximation of the real wing structure behaviour. The Figure 13 and Figure 14 show the general layout of an aircraft wing structure and its most important components.

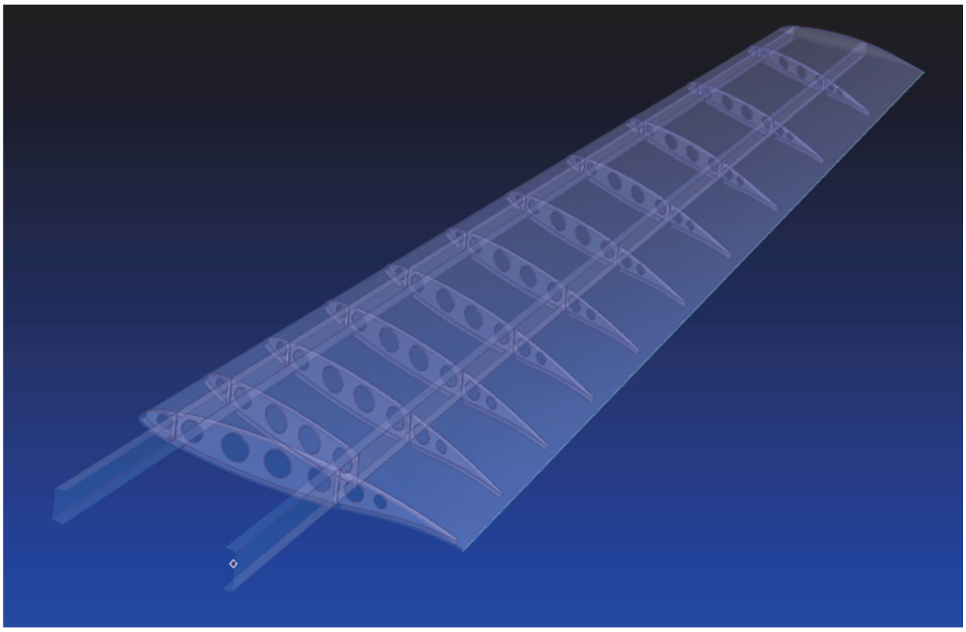

Figure 13 WT FEM model

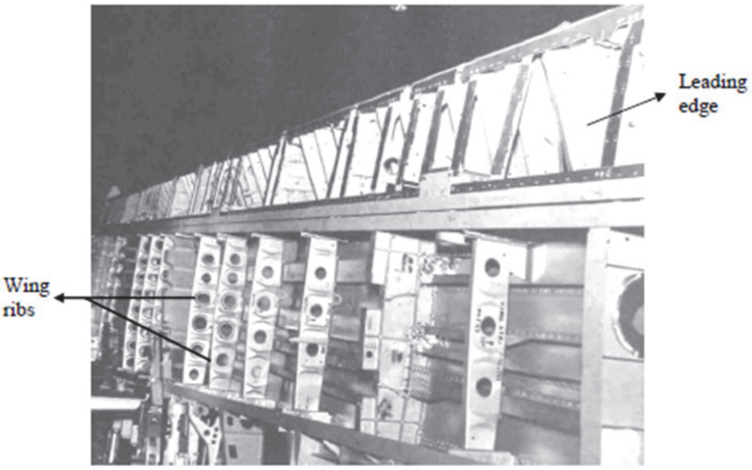

Figure 14 727 aircraft wing with the lower skin not installed showing the wing ribs

Aircraft wing consists of a collection of basic structural elements like ribs (positioned at a different stations along the spanwise direction), front and rear spars and upper and lower wing skins covering these internal components. Considering each element singularly and simplifying their behaviour, spars act as bending elements, skins as torsion members and ribs are used to keep the shape.

In reality, aircraft loads are in the form of air pressure (or suction) on the skin, concentrated loads from the landing gear, power plants, passenger seats, etc. These loads are to be collected locally and transferred to the major load carrying members. This should be done with proper care, otherwise these loads may produce excessive local deflections that are not permissible from aerodynamic considerations.

The skin is thin and has little bending stiffness to resist air pressure. To avoid incurring large deflections in the skin, it is connected to more rigid ribs. They also collect all transverse loads and transfer them to the two wide-flange beams (spars) that are signed to take transverse shear load. The local-to-global load transfer is thus complete.

The main function of the wing is to pick up the air loads and transmit them to the fuselage. The wing cross-section takes the shape of an airfoil, which is designed based on aerodynamic considerations. The wing as a whole performs the combined function of a beam and a torsion member.

The spar is a heavy beam running spanwise to take transverse shear loads and spanwise bending. It is usually composed of a thin shear panel (the web) with flanges at the top and the bottom to take bending.

To withstand high surface air loads and to provide additional bending capability to the wing box structure, thicker skins are often necessary.

Wing ribs are planar structures capable of carrying in-plane loads and are placed along the wing span. Besides serving as load redistributors, ribs also hold the skin to the desired contour shape.

As literature suggests, there are two different procedures often used to project a rib. The first method is designing the wing rib as a shear resistant plate girder that will not buckle nor yield under the applied load. This method is used for the design of the lightly loaded ribs where the we stiffeners are omitted and instead a series of standard flanged lightening holed are introduced. The second method represents a methodology for the design of a wing rib subjected to moderate to heavy loads (bulkheads). The second method is based on the incomplete diagonal tension theory. Designing a rib subjected to heavy loads to act as a shear resistant plate girder will produce a very massive rib. Instead the thickness of the rib will be reduced to the limit to keep it within the elastic deformations limit but with less buckling resistibility where the rib is forced to be under incomplete diagonal tension field stresses. Uprights are introduced to the rib to support rib buckling.

A wing rib extends from the leading edge to the trailing edge of the aircraft wing, thus it can be divided into three main parts, namely the leading and the trailing edges rib portions and the wing box rib portion. Between the three portions, the front and the rear spars are accommodated where the rib is riveted into its webs, as shown in Figure 15.

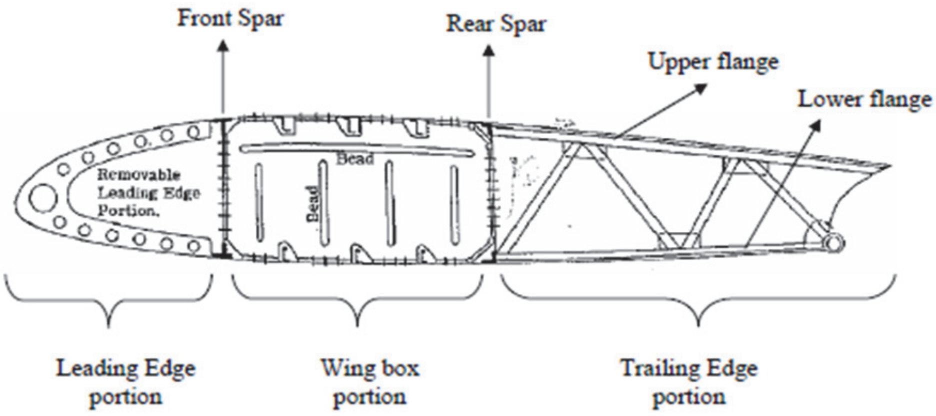

Figure 15 Wing rib Construction

The assembly of the rib with the wing skin-stinger panels has different configurations. The rib may be riveted, spot welded or glued to the skin along its boundary as shown in Figure 16.

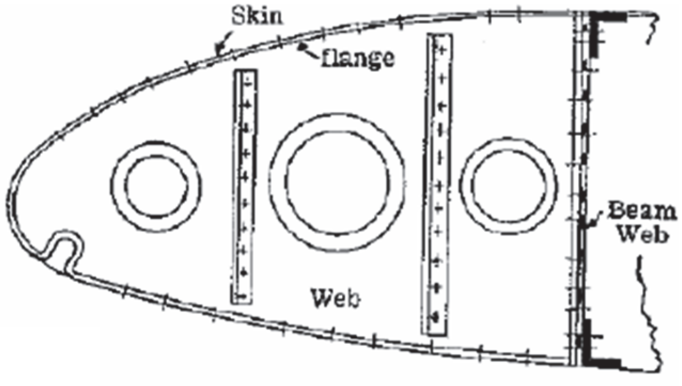

Figure 16 Leading edge wing rib-skin assembly by riveting

In some other cases the rib is notched to host the stingers, as shown in Figure 17 where the lower flange of the rib is notched to host the stringers of the lower skin,

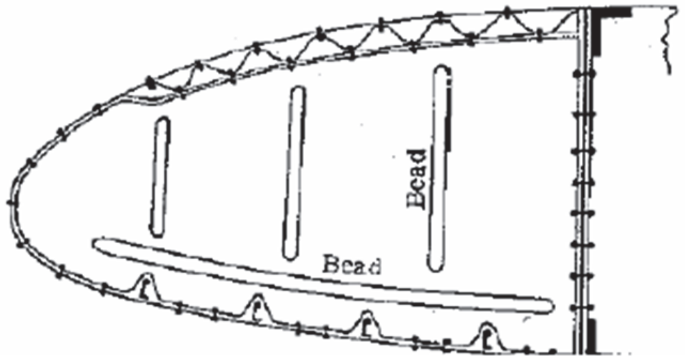

Figure 17 Leading edge wing rib-skin assembly

Lightening holes may be introduced to the web of the rib mass reduction, accessibility and to form a passage for wiring and fuel pipes. Different kinds of ribs and different rib assemblies are required in the aircraft design. Since the ribs compose an appreciable part of the wing, an accurate design for the wing rib that guarantee the necessary strength with minimum weight.

The pressure variation along the chord length results also in a variation in the lift force distribution along the chord, which by its role changes the resulting shear forces and bending moments acting on the rib cross-section, as shown in Figure 18. In the paper quoted here, the resultant lift forces acting on certain cross-section along the wing span will be considered as concentrated force acting at the quarter chord length.

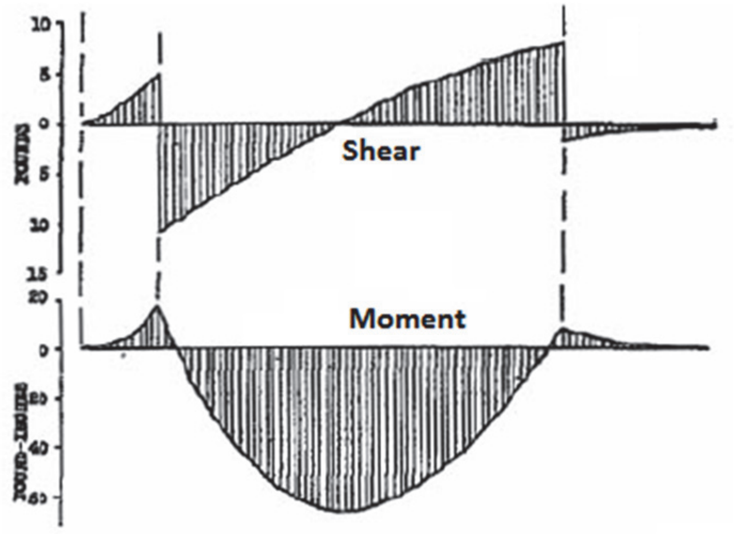

Figure 18 General representation of the shear force and bending moment distribution acting on a wing rib

All these external aerodynamic loads will be resisted by internal reactions in the wing structure. The design of the stiffened panels is based on the assumption that the stringers are the members which are responsible about the bending resistance, while the skin is designed to just carry in plane stresses in the form of in plane shear stresses and tensile stresses, but its resistance to compressive stresses is very limited due to its instability under slightly compressive loads. The variation of the bending stress along the stiffened panel will generate a flexural shear flow in plane of the airfoil.

Unsymmetrical beam sections are very common in aircraft structure, because the airfoil shape is generally unsymmetric. Considering a transversal load P acting on an unsymmetric cross-section passing through its shear center (so that the section is free of twisting).

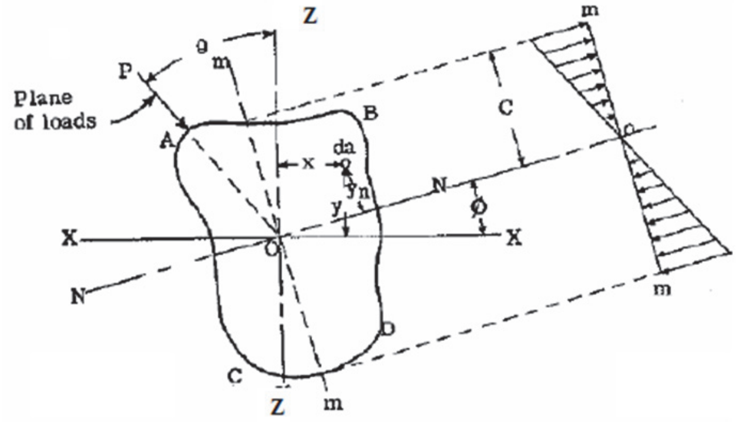

Figure 19 Unsymmetrical cross-section of a straight cantilever beam

Since this is an unsymmetrical cross-section beam, it is expected that its cross.-section will warp under the effect of bending shear stresses, according to Saint-Venant’s theory, but for simplification it is assumed here that the section is restrained of warping. The equation of the bending stress in beams with unsymmetrical cross-sections, based on simple beam theory is:

$$\sigma_b = -\frac{(M_x I_z - M_z I_{xz})}{I_x I_z - I_{xz}^2} z - \frac{(M_z I_x - M_x I_{xz})}{I_x I_z - I_{xz}^2} x \,;$$

Based on this equation, there are four methods, so far, for the derivation of the shear flow equations in beams with unsymmetrical cross-sections subjected to flexural shear stress namely:

- The principle axes method;
- The neutral axis method;
- The K-Method;
- The ΔP-Method.

The first three methods are dedicated for beams with unsymmetrical but constant cross-sections along its span, i.e. its inertia moments are constant along the span while the fourth one is dedicated for beams with unsymmetrical and inconstant cross-sections (tapered sections). Following a brief description of each method:

- Principle axes method.

This method is used for the calculation of the shear flow in beams with unsymmetrical but constant cross-sections. It is based on the calculation of the shear flow due to principle stresses. It is known that the product area moment of inertia I_{xz} is zero with respect to the principle axes, then σ_b equation becomes:

$$\sigma_b = -\frac{M_{xp}}{I_{xp}} z_p - \frac{M_{zp}}{I_{zp}} x_p \; ;$$

From this equation. The equation of the shear stress acting on the cross-section will be

$$\tau_b = -\frac{V_{zp}}{I_{xp} t} \int z_p dA - \frac{V_{xp}}{I_{zp} t} \int x_p dA \; ;$$

Where $\int z_p dA$ and $\int x_p dA$ are the first moment of area with respect to the X-X and Z-Z axes respectively and t is the thickness of the beam. These area moments of inertia can be calculated by superposition in case of composite cross-section areas.

From the last equation the shear flow in the cross-section can be expressed as

$$q_p = -\frac{V_{zp}}{I_{xp}} \sum z_p A - \frac{V_{xp}}{I_{zp}} \sum x_p A \, ;$$

- Neutral Axis Method

This method is used for the calculation of the shear flow in beams with unsymmetrical but constant cross-sections. It is based on the calculation of the shear flow due to stresses about the neutral axis of the cross-section N-N. simply, by resolving the stress obtained in method one into the neutral axis direction, the equation of the bending stress becomes:

$$\sigma_b = \frac{M_n z_n}{I_n} \; ;$$

Where $I_n = I_{xp} \cos^2(\alpha) + I_{zp} \sin^2(\alpha)$, $z_n = z \cos(\phi) - x \sin(\phi)$ and $\tan(\alpha) = -\frac{I_{xp}}{I_{zp}} \tan(\theta)$ where θ is the angle formed between the transversal load and the Z axis while α is the angle between the neutral axis and the X-X axis. From the σ_b equation, the shear flow expression can be written as:

$$q_n = \frac{V_n}{I_n} \sum z_n A$$

Where V_n is the shear force in the N-N direction.

- K-Method

This is the most widely used method for the calculation of the shear flow in beams with unsymmetrical and constant cross-sections. From the general equation for σ_b it is possible to derive the equation of the flexural shear flow in the form

$$q = -(K_3 V_x - K_1 V_z) \sum xA - (K_2 V_z - K_1 V_x) \sum zA\,;$$

Where $K_1 = \frac{I_{xz}}{I_x I_z - I_{xz}^2}$, $K_2 = \frac{I_z}{I_x I_z - I_{xz}^2}$ and $K_3 = \frac{I_x}{I_x I_z - I_{xz}^2}$

- ΔP-Method

In airplane wing and fuselage structures, the common case is a beam of non-uniform section in the flange (stringer) direction. Figure 20 shows a single cell distributed flange beam. Consider the beam acts as a cantilever beam with the bending moment existing at section (A) being greater than that existing at section (B) and that the bending moment produces compression on the upper surfaces. Using the general equation for σ_b, the bending stress on each stringer can be found which if multiplied by the stringer area gives the stringer axial load, as shown in the figure. imagine the upper sheet panel 2-2’-3-3’ is cut along the line a-a. Furthermore consider stringer number 3 cut out and shown as a free body in Figure 21.

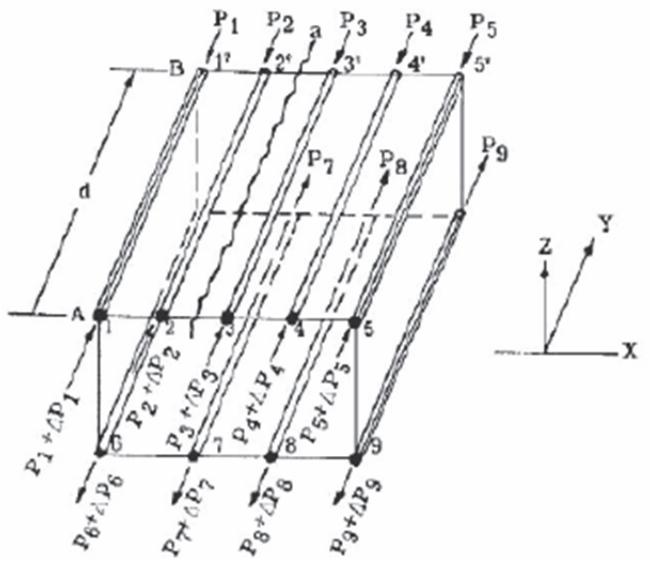

Figure 20 Non-uniform beam cross section

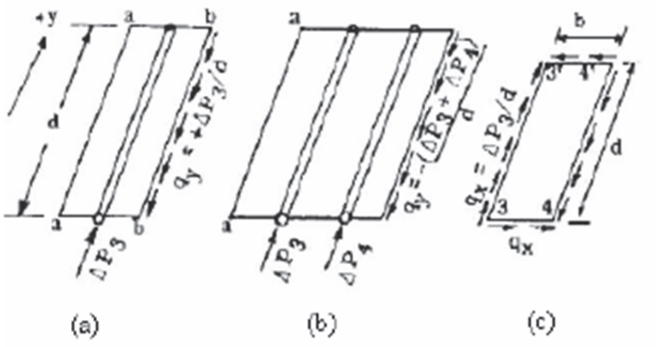

Figure 21 Free body diagram of panels

Let q_y be the average shear flow per inch over the distance d on the sheet edge bb. For equilibrium of this free body, $\Sigma F_y=0$, hence $\Delta p_3 + q_y d = 0$ then, $q_y = -\Delta p_3/d$.

Figure 21.b shows a free body diagram including two stringers or flange members. Again writing equilibrium in y direction gives q_y is known, the change in the average shear flow to some other section equals,

$$q_y = -\sum \frac{\Delta p}{d} \;\; ;$$

If the summation is started where q_y is zero then the equation will give the true average shear flow q_y. Then the shear flow in the section at point 'n' can be represented generally as

$$q_{y_n} = q_0 - \sum_{i=1}^{n} \frac{\Delta p_i}{d} \ ;$$

Figure 21.c shows sheet panel 3-3’-4-4’ isolated as a free body. Taking moments about corner 4’ and equating to zero for equilibrium, gives $\sum M_{4'} = \frac{d(\Delta p_3)b}{d} - q_x bd$ where $q_x=\Delta p_3/d$. thus for rectangular sheet panels between flange members the shear flow q_x or q_z equals the average shear q_y. To find out how to calculate the section centroid, the section moments of inertia and the shear center coordinates the reader can refer the article here described.

To calculate external loads on the portion of wing to be designed, it is useful to divide them in 3 categories:

- Vertical shear force V_Z^j:

This vertical shear force includes:

i. The total lift summation from the wing tip until the j^{th} wing station which can be obtained from aerodynamics considerations. This value of shear force must be multiplied by maneuvering condition factor plus safety factor for load and calculation tolerances.
ii. Wing structural weight (body forces) included in the wing portion extending from the wing tip until the j^{th} station. It is important to note that in the conceptual design stage the size of the wing parts is not yet determined. Accordingly, the weight of the wing portions will not be available. Alternatively, an approximate value for the distribution of the wing weight along the wing span can be obtained from previously designed airplanes, or the weight may not be included in the initial sizing process, then it can be included later so that an iteration design process can be conducted for a suitable convergence for the wing weight.
iii. Inertia forces (body forces), where the mass of the wing portion structure must be multiplied by the acceleration of flight in the vertical direction.
iv. Non-structural mass forces due i.e. to the fuel tank weight in the form of weight and inertia forces.

- Horizontal shear force V_X^j

This horizontal shear force includes:

i. The total rag summation from the wing tip till the j^{th} wing station. This value of the drag force obtained from wind tunnel calculations must be multiplied by maneuvering condition factor plus safety factor.
ii. Inertia forces (body forces), where the mass of the wing portion structure must be multiplied by the acceleration of flight in the horizontal direction.
iii. Non-structural mass forces due i.e. to the fuel tank weight in the form of inertia forces.

- Twisting moment

As previously defined the wing station is subjected to twisting moment M^j the sources of this twisting moment are

i. The pitching moment M_{qc}^j. The pitching moment about quarter chord location can be obtained from aerodynamic considerations. It is important to note that the value of the pitching moment so defined must be multiplied by a factor of safety as well as a maneuvering conditions factor to obtain design loads.
ii. Twisting effect of lift forces. The lift force is always calculated with respect to the aerodynamic center of the sing cross section which with an acceptable approximation considered as the airfoil quarter chord location. This lift force at the quarter chord has a twisting effect with the value of $V_Z^j e_{Xj}$.
iii. Flange forces twisting moment M_f^j. But the aircraft has a tapered wing, the stiffeners are not perpendicular to the airfoil cross-section but they have inclination angle in the Y-Z plane as well as in the Y-X planes. These inclinations generate a flange force components in the three directions $F^j_{fX,I}$, $F^j_{fY,I}$ and $F^j_{fZ,i}$. These forces are generating a flexural shear effect as well as a twisting effect on the airfoil cross-section.
iv. Twisting effect of the drag forces. If the line of action of the drag forces is not passing with the airfoil shear center, then a twisting effect takes place with magnitude $V_X^j e_{Zj}$.
v. Twisting effect wing portion weight. Once the wing weight included in the design process, a twisting effect of the wing portion weight must be introduced, the magnitude of this twisting moment is $W_j e_0$ where W_j is the weight of the wing portion extending from the

wing tip until wing station j and e_0 is the horizontal distance between the airfoil centroid and shear center at that wing station.

Other interesting design considerations in the article concern the uprights. An upright is a stiffener that is introduced to the web to oppose the tendency of the diagonal tension strips to pull the upper and the lower flanges together. It may be in the form of a stiffener member, double on both faces of the web or single on one side of the web. In both cases and since it is subjected to compressive stress, a buckling analysis should be conducted to insure that it will be stable under the compressive load.

The traditional buckling analysis of columns cannot be applied directly to the upright, since the upright is fastened into the web or a built-in part of the web as in the case of the vertical beads. But the analysis should be modified because once the upright starts buckling, it will be subjected to a distributed transversal load acted upon from the diagonal tension field strips, trying to turn it back into the plane of the web. The magnitude of this restoring load is proportional to the deflection of the upright.

Concerning rib's design procedure, ribs can be classified according to their type of loading. For example, a rib subjected only to aerodynamic loads is always considered as a lightly loaded while a rib subjected to concentrated forces transferred to its structure from fuel tanks supporting points, control surfaces supporting points (flaps, ailerons etc), armament supporting points (and so on) is considered a moderately loaded rib. A heavily loaded rib which is always referred to a bulkhead is one subjected to concentrated forces transferred to its structure from landing gears and power plant nacelles supporting points.

The design procedure of the wing rib depends mainly on its type of loading as well as some constraints that should be satisfied in the design process (like the requirements of cut outs for the inspection holes and wiring and piping passages though the wing)

Although the ideal design for the wing rib is designing for incomplete diagonal tension state which is efficient from the point of view of weight saving but sometimes the existence of cut outs prevent the design for the diagonal tension case.

Chapter 4 Wind tunnel model setup

In this chapter will be described the procedures for the acquisition of the geometry and the preparation of the analysis. The steps to have a correct model ready to be analyzed are:

- Model acquisition;
- Mean surfaces extraction;
- Choice of the connecting method;
- Meshing the model;
- Load transfer.

In Chapter 5 there will be the description of the checks performed to prevent any data loss during the acquisition step.

Acquisition and transfer of the model

The first step to be done is a correct acquiring procedure. The model was drawn and aerodynamically designed in different industrial softwares.

First of all, several saving format were tried to export from Catia5 to SolidWorks 2013 (CAD to CAD transfer), the .iges format was found to be the best one. The Initial Graphics Exchange Specification (IGES) file format standard was developed to address the incompatibility issue with various CAD/CAM systems. This standard allows efficient and accurate exchange of product definition data across almost all CAD/CAM systems. An IGES file is composed of 80-character ASCII records, a record length derived from the punch card era.

After the operations in SolidWorks were performed, another transfer issue has to be dealt with. This time the transfer is from SolidWorks and FEMAP (CAD to FEM) so that the .iges format doesn’t result to be adequate anymore. A correct exportation format is found to be .x_t (Parasolid format). Parasolid's capabilities include model creation and editing utilities such as Boolean modeling operators, feature modeling support, advanced surfacing, thickening and hollowing, blending and filleting and sheet modeling. Parasolid also includes tools for direct model editing, including tapering, offsetting, geometry replacement and removal of feature details with automated regeneration of surrounding data. Parasolid also provides wide-ranging graphical and rendering support, including hidden-line, wireframe and drafting, tessellation and model data inquiries. When exported from the parent software package, a Parasolid commonly has the file extension .x_t. Another format is .x_b, which is in binary format so it is more machine independent and not subject to binary-to-text conversion errors. Most Parasolid files can communicate and migrate only 3D solids and/or surface data. Parasolid files currently cannot communicate and migrate 2D data (such as lines and arcs).

Mean surfaces extraction

To obtain the mean surfaces model three different ways were tried:

- FEMAP *Geometry, Midsurface* commands;
- FEMAP offset commands;
- SolidWorks offset commands.

As first attempt, the FEMAP *Midsurface* command were performed. The midsurfacing commands are available when using the Parasolid geometry engine. They are useful for generating surfaces from thin-walled solid geometry (such this model is). In FEMAP there is also the opportunity to use an offset command. If the offset distance is set to half element's thickness it gives the mean surface as output. Unfortunately, both FEMAP's methods here described are quite inaccurate when dealing whit high curvature gradient (such, for instance, is skin's leading edge), resulting in incorrect mean surfaces extraction. As visible in the zoomed Figure 22, surfaces aren't matching.

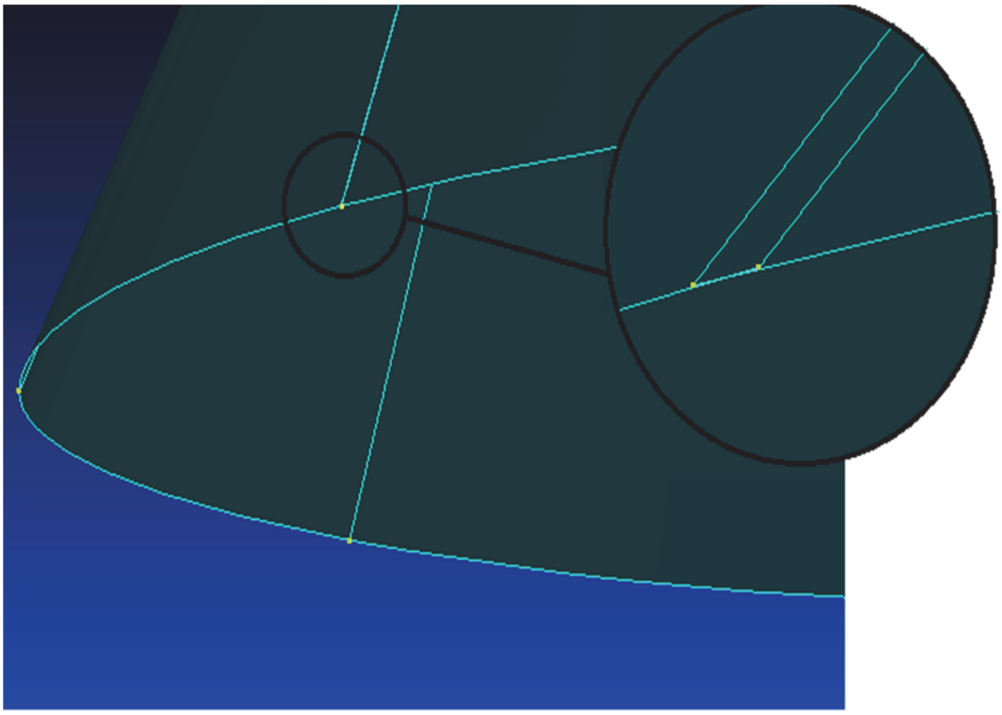

Figure 22 Incorrect mean surface extraction

Instead, even if SolidWorks hasn't got any midsurface tool, it is possible to correctly extract mean surfaces offsetting external (or internal) surfaces by half the thickness. This way a full model composed by mean surfaces is ready for further analysis.

Connection between wing box's elements

Once the mean surfaces are found, model's elements result to be unlinked between each other. But the mean surfaces are found from a solid model, the gap between elements is equal to the sum of half the thickness of two adjacent parts.

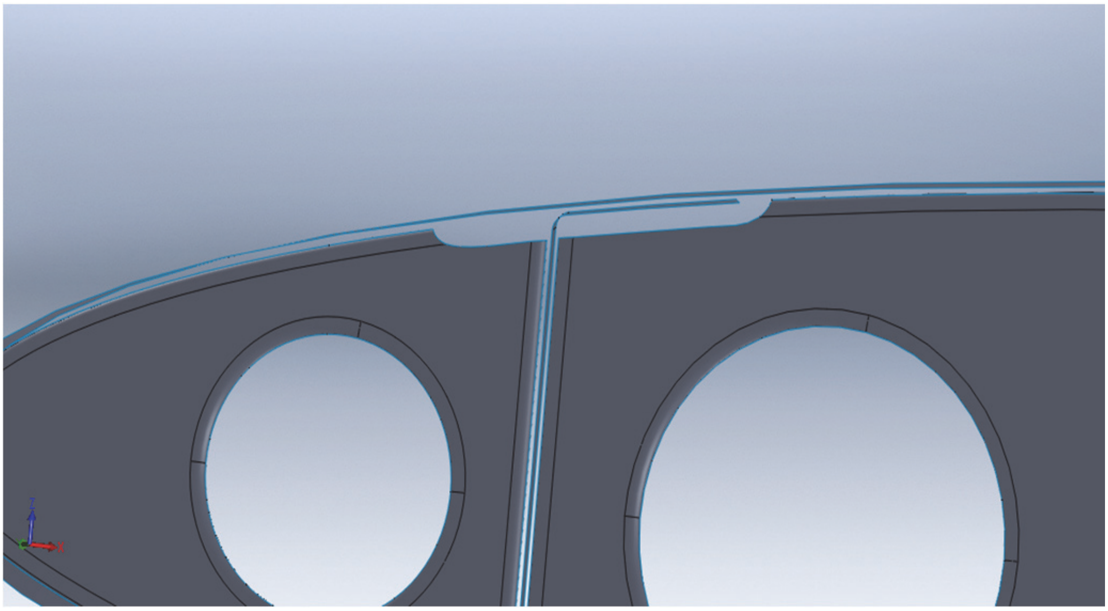

Figure 23 Gap between elements' mean surfaces

In order to connect the elements of this model two different strategies are followed so that is possible to confront their results and to choose the better one. The commands used, available in FEMAP, are *Connect, Surfaces* and *Mesh, Connect, Closest Link*.

- *Connect, Surfaces*. This command allows to connect two surfaces between each other so that the relative displacements are bonded. The way this connection works is defined by the connection *Property.* The *Connection Type* chosen for the property is the *Glued* one. The command actually pastes the surfaces together, acting as an internal clamp.
- *Mesh, Connect, Closest Link.* This command is used to connect stiffly two nodes (or set of nodes) in order to have them moving together. It's a mesh based command, so its effectiveness depends both on quality and on matching of the meshes to be connected.

In order to compare the strategies two different, simplified models are realized. The first one consists of the front part of a rib and the adjacent part of a spar; the second one consists of a whole rib and adjacent slices of skin and spars (Figure 24).

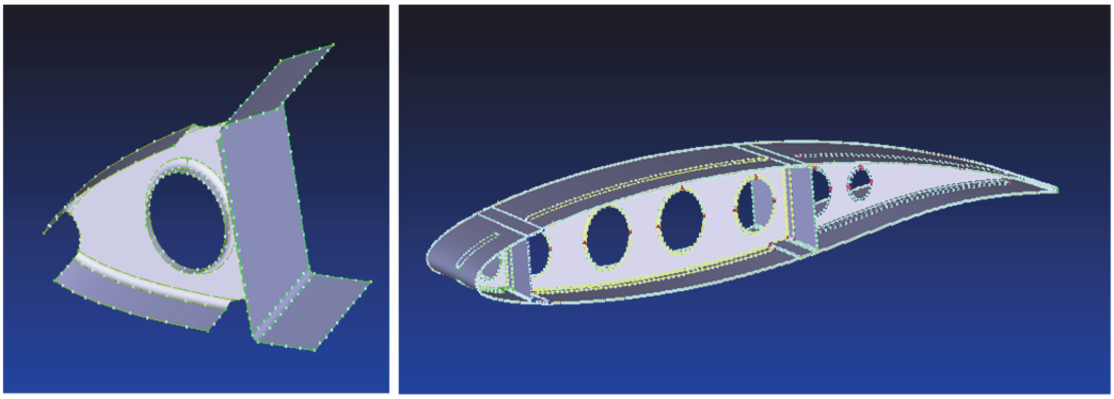

Figure 24 Simplified testing models.

The meshing is done in both models using plate, triangular (3-nodes) elements (steel whit thickness t= 0.5 mm).

The fist model is clamped on the upper and lower spar's edges and loaded on the hole with nodal forces (perpendicularly to rib's surface).the results of the analysis are shown in the figure below: in the left side the Glued type, in the right one the Linked type (whose stiff connecting elements are clearly visible at the rib-spar interface). The shown values are Von Mises stresses.

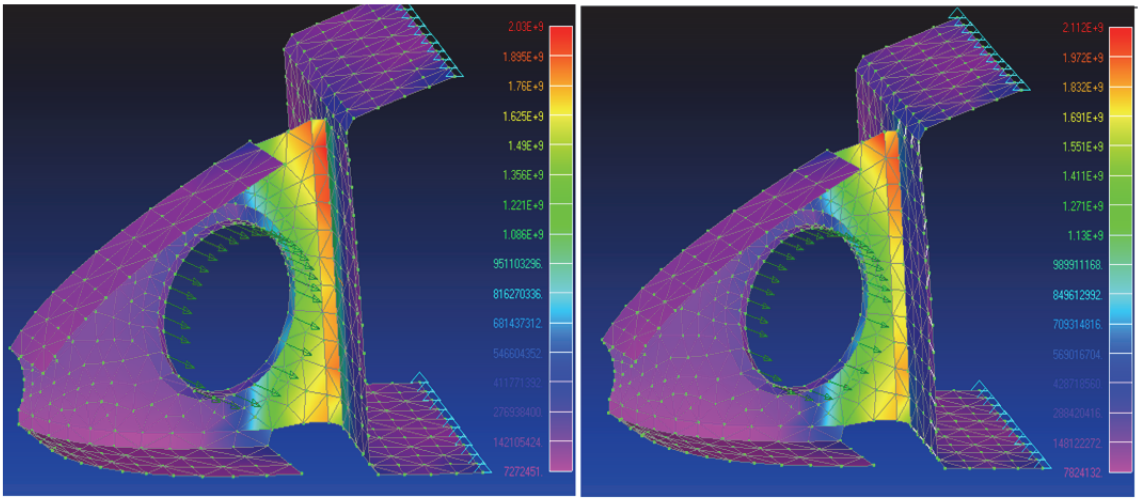

Figure 25 *Linked* model vs *Glued* model

The second model is clamped on the inferior bases of spars and loaded on a portion on the superior skin by nodal, traction forces. Figure 26 and Figure 27 show the loaded zone and bonded zone.

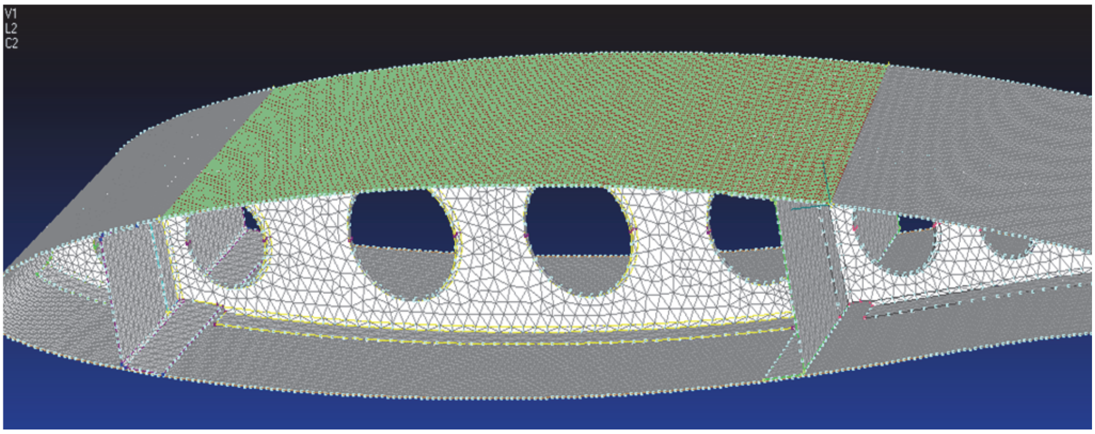

Figure 26 Loaded zone

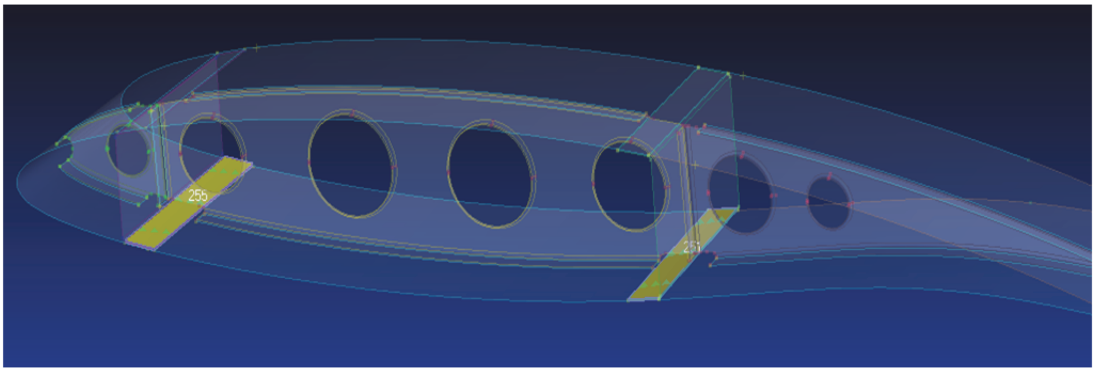

Figure 27 Fixed zone

The results are shown below (*Glued* upside and *Linked* downside). The value shown is the total displacement. Despite both loads and bonds are symmetric to the vertical rib's surface the displacement field isn't symmetric at all. This happens because rib's cross section is C-shaped so one side of the model is less stiff than the other one.

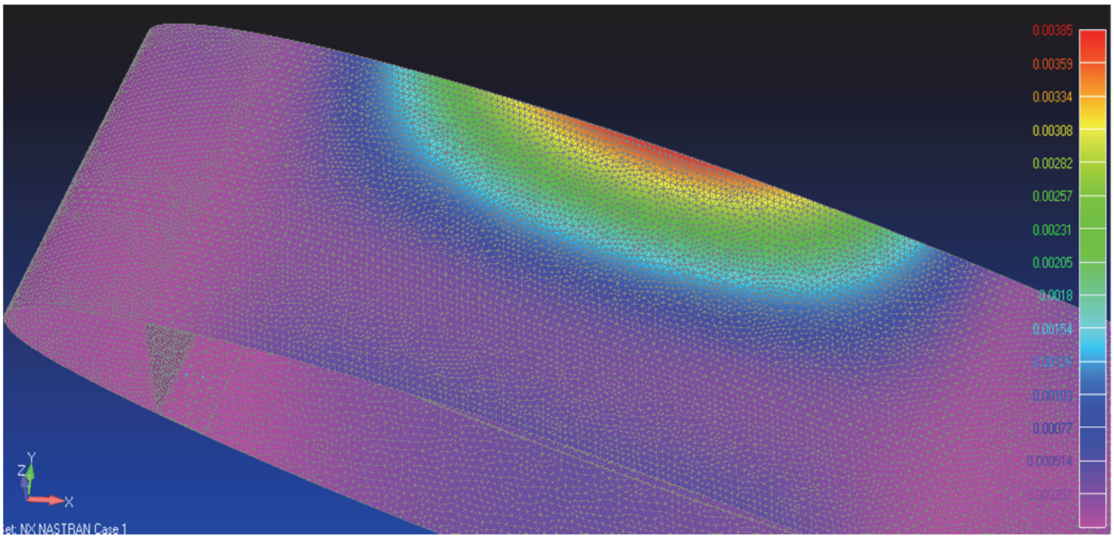

Figure 28 Glued model

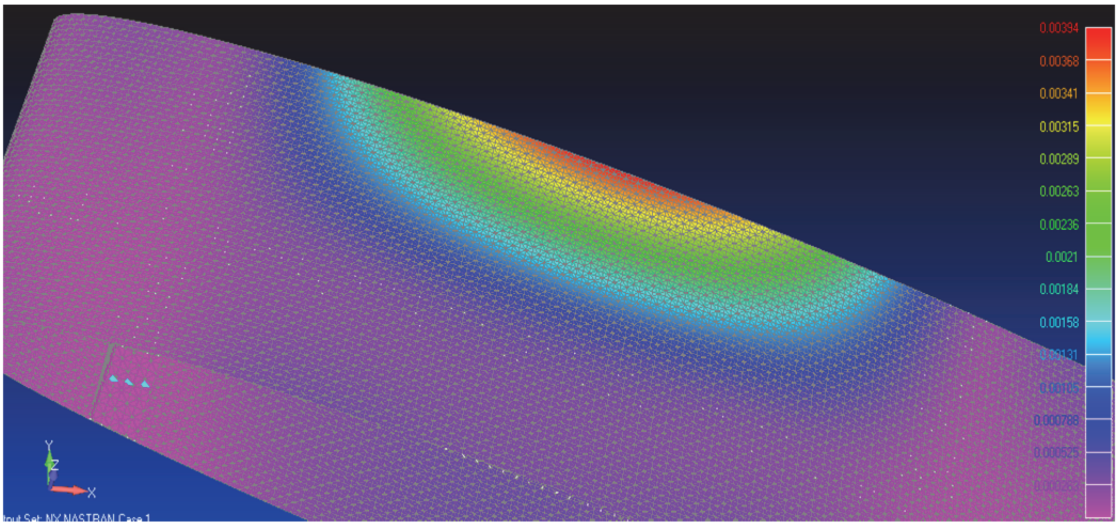

Figure 29 Linked model

Modeling choice.

As clearly stated by these cases, the results are almost the same (≈4% difference in the first model, ≈2% in the second one). The only important difference between these connection types is that to correctly connect elements with the *Closest Link* command is mandatory to have a matching mesh so that bonded nodes represent the real model as close as possible. Moreover, *Closest Link* command links every node belonging to the first set to the nearest of the second one; so it can happen that a node is bonded to move together with two or more nodes that have different displacements (resulting in the analysis to fail). A feature to take into account while using the *Connect, Surfaces* is that this method is computationally onerous, so it is needed to slice the target surface with the starting surface's profile in order to minimize runtime (Figure 30).

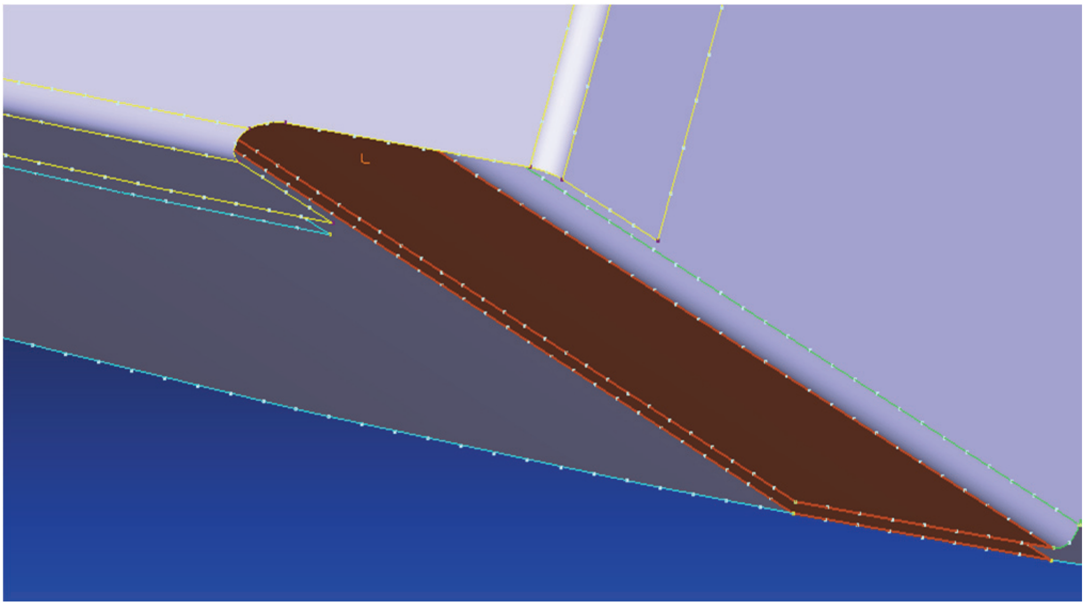

Figure 30 Example of a *Glued* zone

The choice of the modeling strategy thus is the *Glued* model because, giving the same results, it is quicker to implement.

Mesh characteristic

The choice of a correct mesh size is mandatory to achieve correct results. It's important to underline that there is not a unique mesh for every simulation problem, instead the mesh has to respect two opposite requirements: being fine enough to represent correctly the shape of the object but also coarse enough to be calculated in relatively brief time. Examples of correct and wrong meshes are shown below (Figure 31).

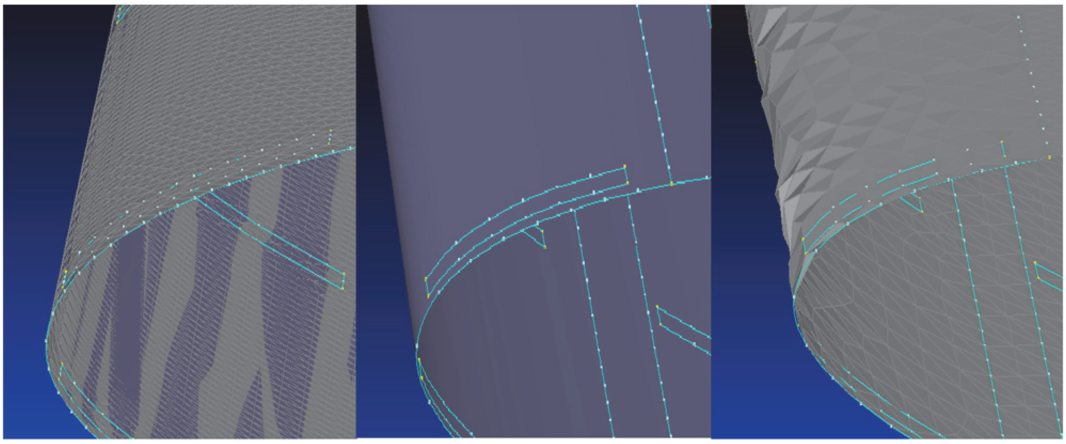

Figure 31 Comparison between correct and incorrect mesh size

After several attempts, an optimal mesh size is found to be 7 mm with a finer mesh (a 4 mm mesh size) on the skin front so that its curvature will be correctly modeled. A mesh of 65204 nodes (126052 elements) is obtained. Using such a mesh size, a correct modeling is performed everywhere; in Figure 32 the mesh of the highest slope gradient zone of the model is shown to be correct. The computational time is less than 2 minutes for static analysis, 7 minutes for buckling analysis and 10 minutes for modal analysis on a i5 quad-core.

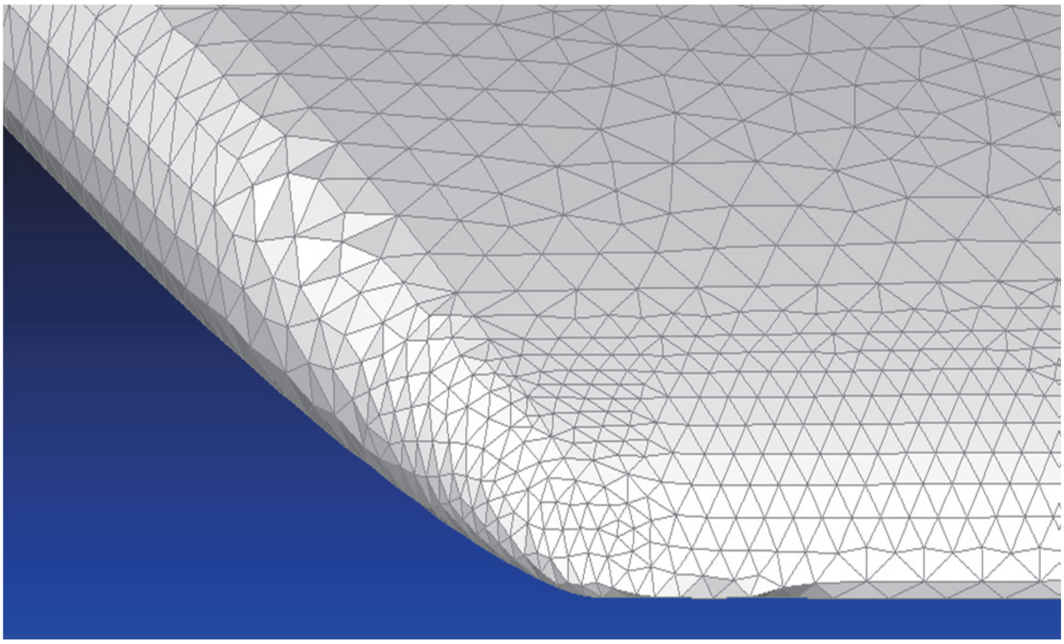

Figure 32 Mesh on a high slope gradient zone

The elements used are plate, triangular (3-nodes) and composed of an aluminum alloy (as the project requires); the thickness is varied according with the static analysis and buckling results, but a first value of t = 0.5 mm is chosen. Typical characteristics for aluminum alloys are E = 70 GPa, ν = 0.34, ρ = 2700 kg.

The element type used to mesh the WT model is CTRIA3. The CTRIA3 element is a constant strain element. Its bulk data entry can be found in this form:

CTRIA3	Element ID	Property ID	Node 1 ID	Node 2 ID	Node 3 ID

Where the last 3 numbers are the grid point identification numbers that identify the elemental nodes in the GRID entry format:

GRID	Node ID	Property ID(0)	X coordinate	Y coordinate	Z coordinate

Transfer of loads

When dealing with multiphysic problems it is very important that a correct data exchange is performed. In this project, the data to be transferred is the CFD load map.

The CFD load map, not developed in this work, has the following border conditions

Table 3

Calculus references	
Mean Aerodynamic Chord MAC	0.495 m
Surface S	0.754 m^2
Density ρ	1.225 kg/m^3
Velocity V	45 m/s
Pressure P	100084.7 Pa
Mach Number Ma	0.132225
Reynolds Number Re	1.525069 10^6

With this values, the results in terms of C_L, C_D and C_M with respect of wing twist angle are:

Table 4

CFD Results					
Wing Twist [degree]	C_L	C_D	C_M	L [kg]	D [kg]
-6	0.0282	119.6	-0.097	2.68833	1.140157
-3	0.306	139.4	-0.0988	29.17124	1.328912
0	0.58	207.8	-0.1007	55.29189	1.980975
3	0.847	322	-0.10388	80.74523	3.069653
6	1.0955	476.4	-0.1049	104.4349	4.541562
8	1.245	601	-0.1043	118.6869	5.729384
10	1.384	754	-0.1047	131.9379	7.187946
12	1.48	923	-0.095	141.0897	8.799037
13	1.2	2200	-0.12	114.397	20.97279

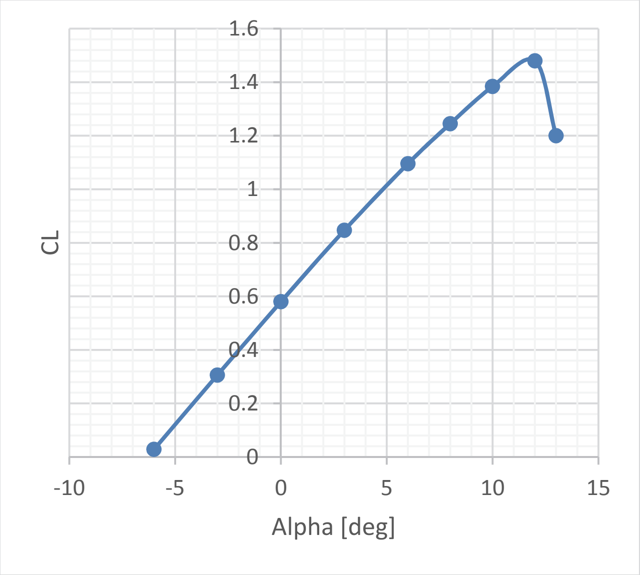

Figure 33 WT model's C_L vs Twist Angle

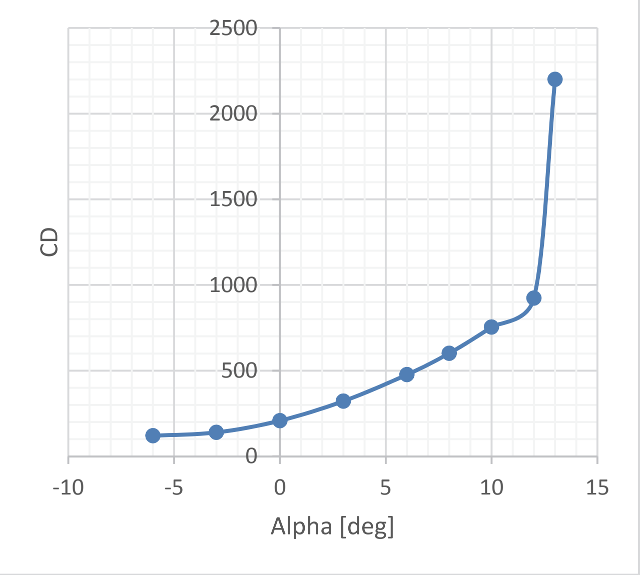

Figure 34 WT model's C_D vs Twist Angle

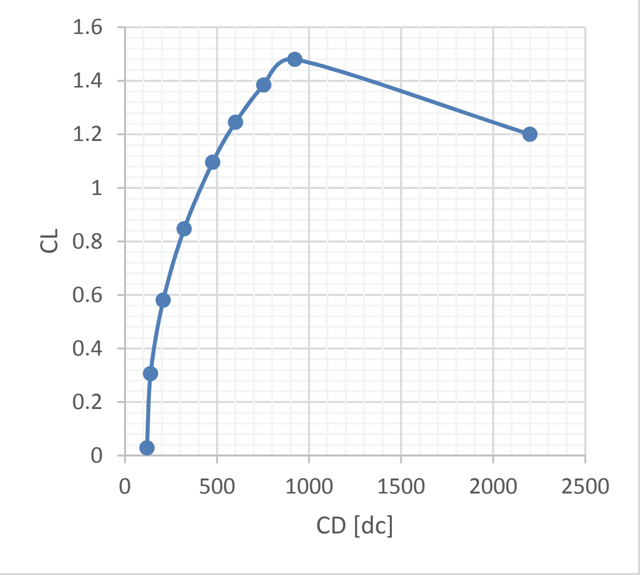

Figure 35 WT model's Efficiency

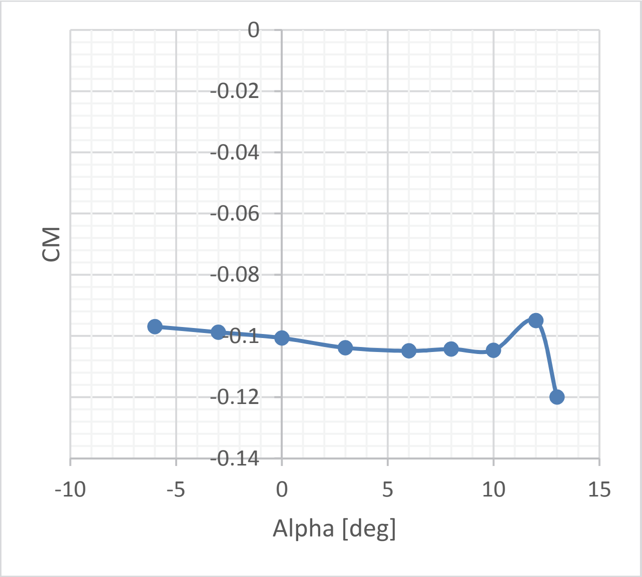

Figure 36 WT model's C_M vs Twist Angle

The design wing twist angle is of 6 degrees. The interaction between air particles and wing’s skin is reported below (the contour shown is pressure distribution):

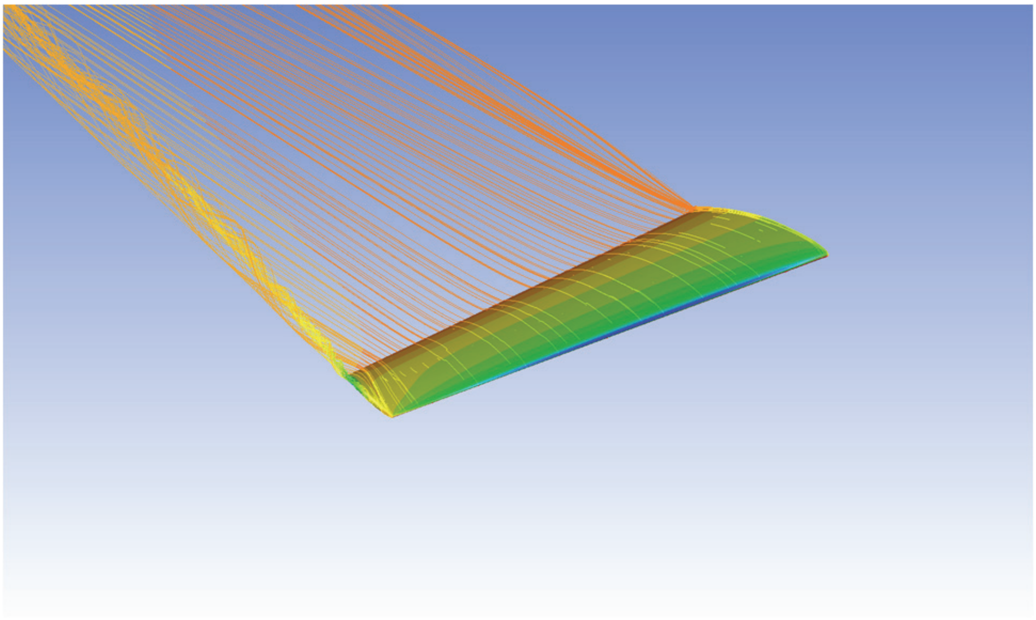

Figure 37 CFD Result

FLUENT gives the opportunity to transfer loads in two different ways, as pressure on elements or force on nodes. After loads are exported (as .bdf files) in FEMAP and a static analysis is performed, resultants from FLUENT and FEMAP can be compared. Both loads type (pressures or forces) result to be too inaccurate. This is probably due to rounding problems: FEMAP works with an 8-bit architecture; so, for instance, a pressure compressive load of 100512 becomes -1,00E+05 so that 512 Pa are lost. Summing these errors for each element brings to a severe accuracy loss (about 30% of the lift).

To prevent such an error, another attempt is done using the RBF Morph load transfer tool. From FLUENT skin's mesh, a load map is created by interpolating pressure values on nodes and on elements' centroid. This result to be an high enough number of source points (shown in Figure 39) to have a correct mapping. Then, it is possible to transfer this pressure map on FEMAP's mesh which, as usual in these problems, isn't matching with the CFD mesh. Loads are transferred as PLOAD4 so that a higher accuracy is achievable (3 pressure values are placed on each element, Figure 38). PLOAD4 bulk data entry can be found in the form:

PLOAD4	Data Set	Element ID	P1	P2	P3

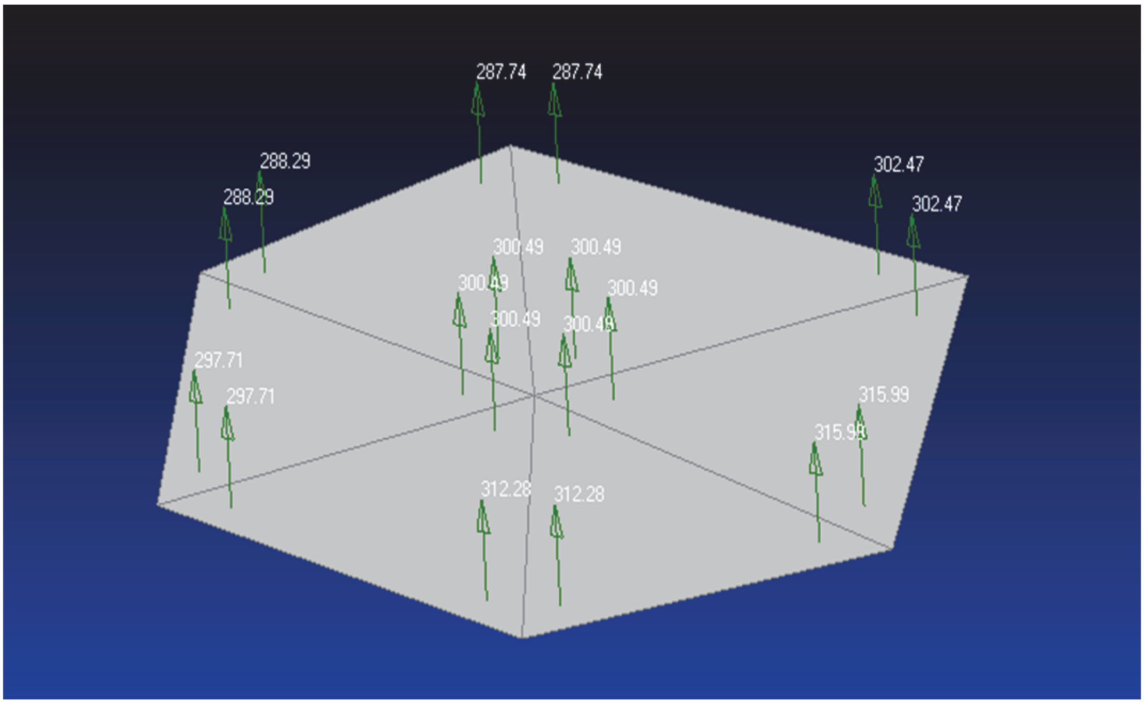

Figure 38 Load distribution on elements

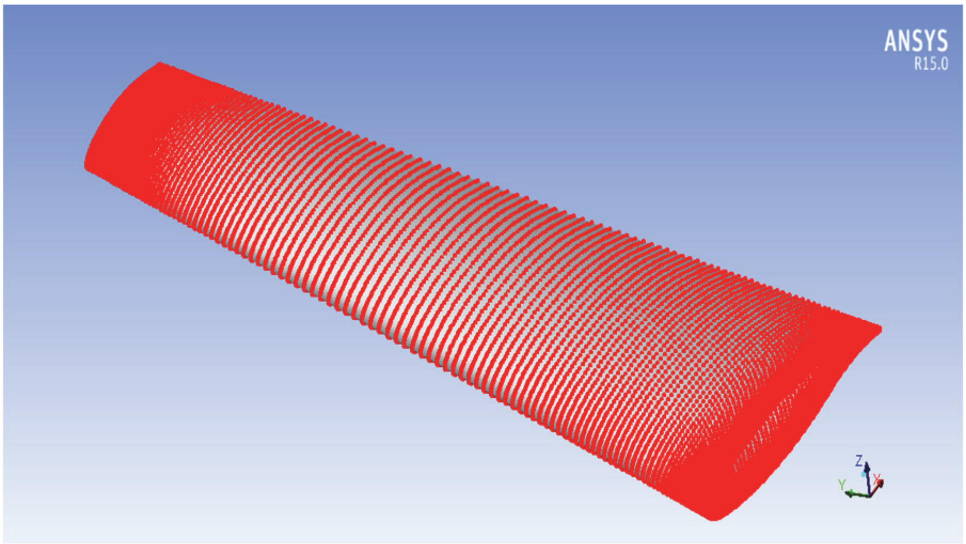

Figure 39 Load Transfer's Source Points

RBF Morph load transfer tool gives the following results:

Table 5

Load Resultants Comparison			
	Lift	Drag	Y Direction
FLUENT	1021.4573 N	88.074789 N	9.4911734 N
FEMAP	998.9685 N	82.41162 N	10.70788 N
Transfer Error	2.2 %	6.4 %	11.3 %

Wind tunnel test

An example of facility suitable to our requirements is the low speed wind tunnel of the university “Federico II” in Naples (Figure 40). To that kind of facility we will refer to setup the test campaign.

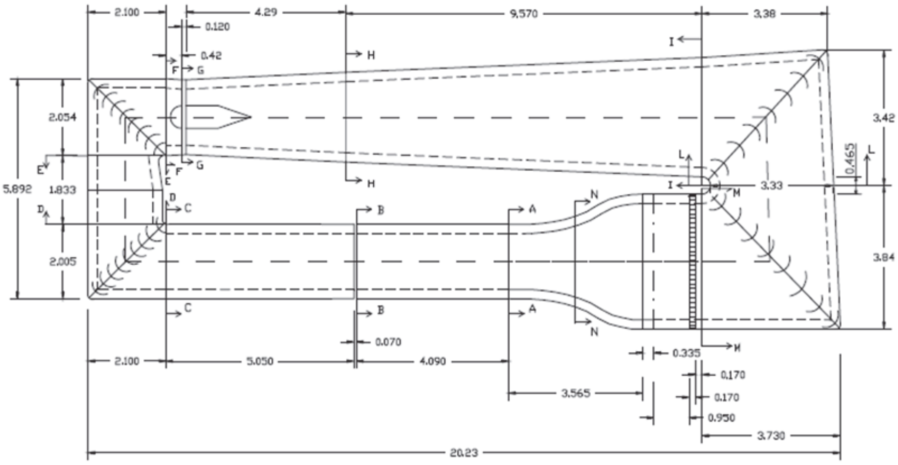

Figure 40 Wind Tunnel layout

The test section is 2 meter wide, the airflow speed limit is 45 m/s and a balances measurement limit is assumed of 100 kg for the lift and 20 kg for the drag. The model will be installed on the side wall of the test section as a cantilever. Its structure will be dimensioned in order to provide a deformation, under the aerodynamic load of 45 kg, which is representative of a realistic deformation that a full scale wing would exhibits in cruising conditions. The dimensioning criteria must also accomplish the safety margin requirements of the facility.

Concerning the model, the skin is divided in three parts: an upper, a lower and a leading edge panel. The lower panel will be joint by screws to allow an easy inspection of the internal installations.

Two lines of pressure taps will be installed at the 30% and at 70% of the model span. A number of 40 are planned to be located at the inner station, 25 at the outer and 15 spanwise on both upper and lower surface. Such a matrix is assumed to be sufficient to validate the pressure distribution estimated by numerical model. Figure 41 reports the map of the pressure taps locations on wing’s skin.

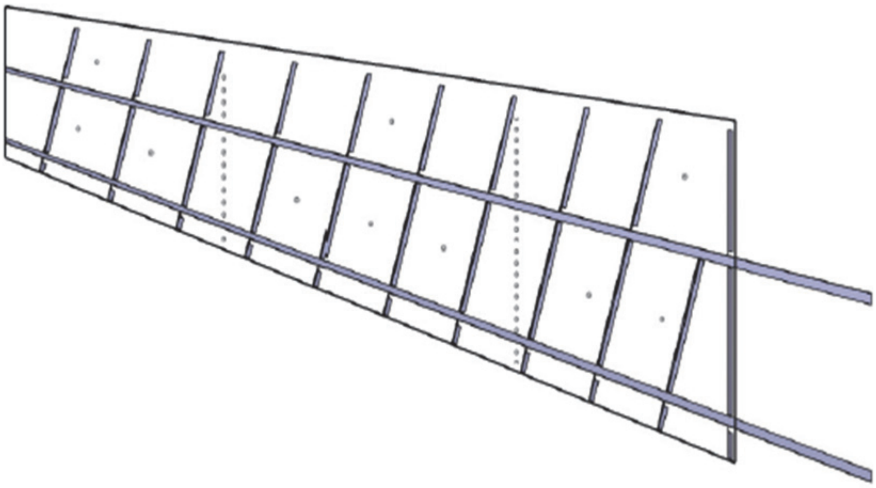

Figure 41 Location of pressure taps

Strain gauges will be positioned in several points on skin, spars and ribs in the most significant locations identified by the FEM analysis.

Analysis tools

In this paragraph a brief description of the way how a FEM software solves typical is given so that results are easily interpretable.

To obtain normal modes, Newton's equation need to be solved:

$$M\ddot{x} + Kx = 0$$

M and K are the mass and the stiffness matrix. Here, the damping matrix C is assumed to be small enough to be neglected. If the solution to be found is in the form of $x_i = u_{0i} \sin(\omega_i t)$, the equation becomes:

$$(-\omega_i^2 M + K)u_{0i} = 0$$

Where ω_i^2 are the eigenvalues and u_{0i} the eigenvectors.

Concerning buckling analysis, equations are to be solved taking into account second order strains; so a new stiffness matrix is introduced, called geometric stiffness matrix K_{geom}, that actually reduces the capability of withstand loads. The matrix K_{geom} is function of the load configuration but not of its entity (if the linear hypothesis is still valid).

Here, the description of the classic buckling calculus is given as solution of an eigenvalue problem. A better buckling calculus is possible by means of a non linear analysis which is however more computationally demanding. Calculus procedure is divided in two parts:

In the first part, an explorative and arbitrary load P* is defined, which has the same configuration of the one leading to buckling failure but has a small modulus (eg unitary); the stresses state is extracted considering second order deformations. From this tensional state, the matrix K_{geom} can be extracted using for example a variational principle. Summing this matrix to the elastic one, the system is completely defined:

$$P = K_{tot}\, u\,;$$

$$K_{tot} = K_{el} + K_{geom}(P) = K_{el} + \lambda K_{geom}(P^*)\,;$$

With

$$P = \lambda\, P^*\,.$$

But the elastic matrix doesn't change with the applied load, the equilibrium problem is written in a form where a proportionality coefficient λ can be highlighted:

$$P = \left[K_{el} + \lambda\, K_{geom}(P^*)\right] x = \lambda\, P^*\,.$$

The buckling load is the one that leads the solution (displacement field x) has a sharp increase associated to an infinitesimal increase of the load. Mathematically, this can be set imposing that the displacement $x = [\,K_{el} +\ \lambda\, K^*_{geom}]^{-1}\, \lambda\, P^*$ becomes infinite. This condition implies that the determinant of the matrix $[\,K_{el} +\ \lambda\, K^*_{geom}]$ is zero (which means that system's stiffness is zero at that point). So the problem is to find the value of λ so that:

$$\det\!\left(\,K_{el} +\ \lambda\, K^*_{geom}\right) = 0$$

Pre multiplying this equation for $K^*_{geom}{}^{-1}$., the problem reduces to the calculus of the eigenvalues of the matrix $\boldsymbol{K}^{*\,\boldsymbol{-1}}_{\boldsymbol{geom}}\,\boldsymbol{K}_{\boldsymbol{el}}$. But the eigenvalues of this matrix are more than one, the searched value for λ is the one that gives the smallest P = λ P* load. So the solution is:

$$\lambda_{crit} = \lambda_1,$$

$$P_{crit} = \lambda_{crit} P^* \,.$$

The deformed configuration of the structure (the failure mode) caused by the buckling effect is given by the eigenvector x_1 of $\boldsymbol{K}^{*\,\boldsymbol{-1}}_{\boldsymbol{geom}}\,\boldsymbol{K}_{\boldsymbol{el}}$ (the one associated to the eigenvalue λ_1).

This is the usual way for the buckling calculation. However is also possible, and sometimes recommended, to calculate the buckling load using a completely non-linear analysis.

The non-linear analysis is done increasing the load at every step and the solution at the equilibrium is calculated; the failure load corresponds to the system loosing convergence so that it is no more able to find a deformation that can withstand applied loads. Others methods (eg Riks analysis) give the opportunity to make a post-buckling analysis so to check that the deformation associated to the collapse will take back a stable configuration.

Concerning optimization analysis, FEMAP optimizer uses Sol200 as solver. In Figure 42 the command windows is showed.

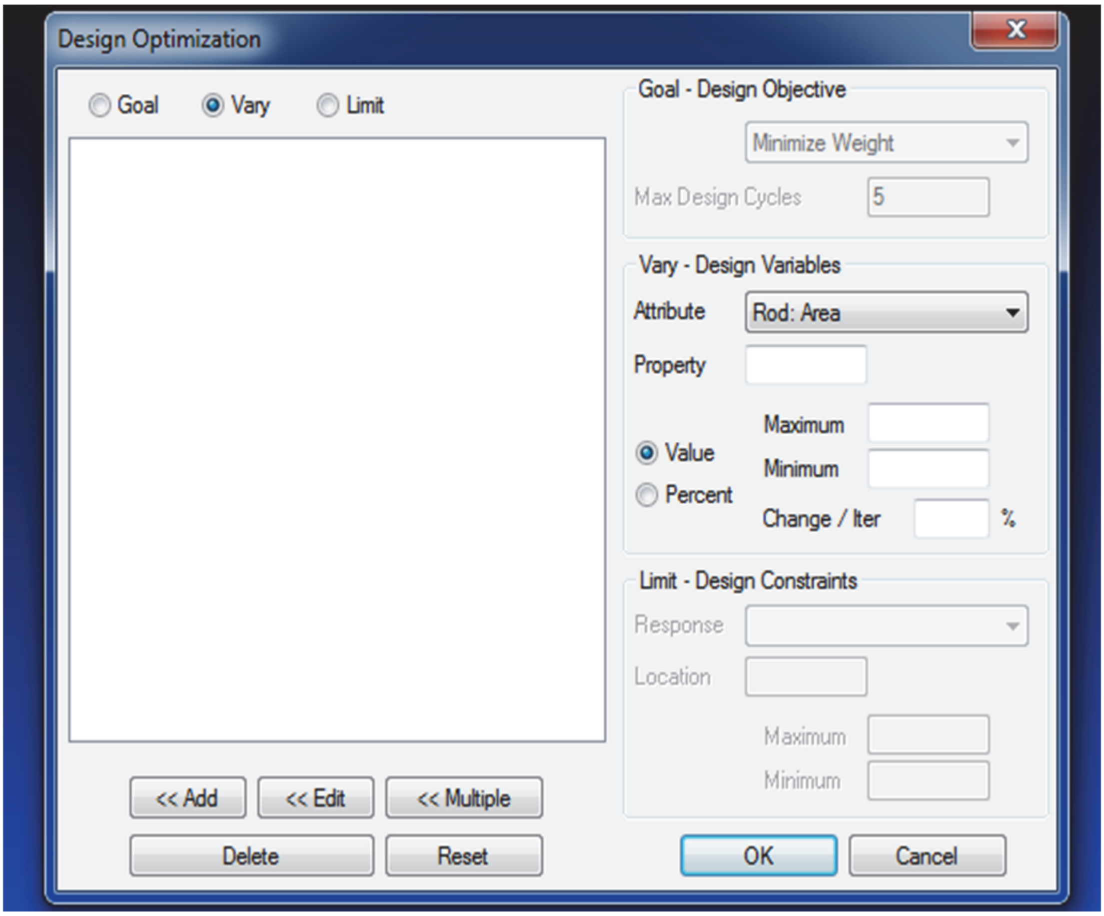

○ Goal ● Vary ○ Limit

Minimize Weight

Max Design Cycles 5

Attribute Rod: Area

Property

● Value ○ Percent

Maximum

Minimum

Change / Iter %

Figure 42 Optimization Command window

Three section must be filled for the analysis to run.

The first one is the Goal – Design Objective in which the only goal available is the weight minimization; the maximum number of cycle can be set, after that value, the analysis will stop. The analysis stops anyway if hard convergence is achieved.

The second section Vary – Design Variables has several fields. Attributes has a list of changeable parameter. This are the parameter to be changed in the optimization process. The attributes depend on the element type. They are:

- Rod: Area;
- Rod: Torsion Constant;
- Bar: Area;
- Bar: I1;
- Bar: I2;

- Bar: Torsion Constant;
- Plate: Thickness.

After the attribute is set, its property ID has to be entered in the Property field. That the variation of the attribute can be chosen. Maximum and minimum values are definable (They can both be set as absolute values or as percentage) as well as the iteration step. The iteration step (Change/Iter) is always a percentage. The Figure 43 shows an example of a Design Variable set.

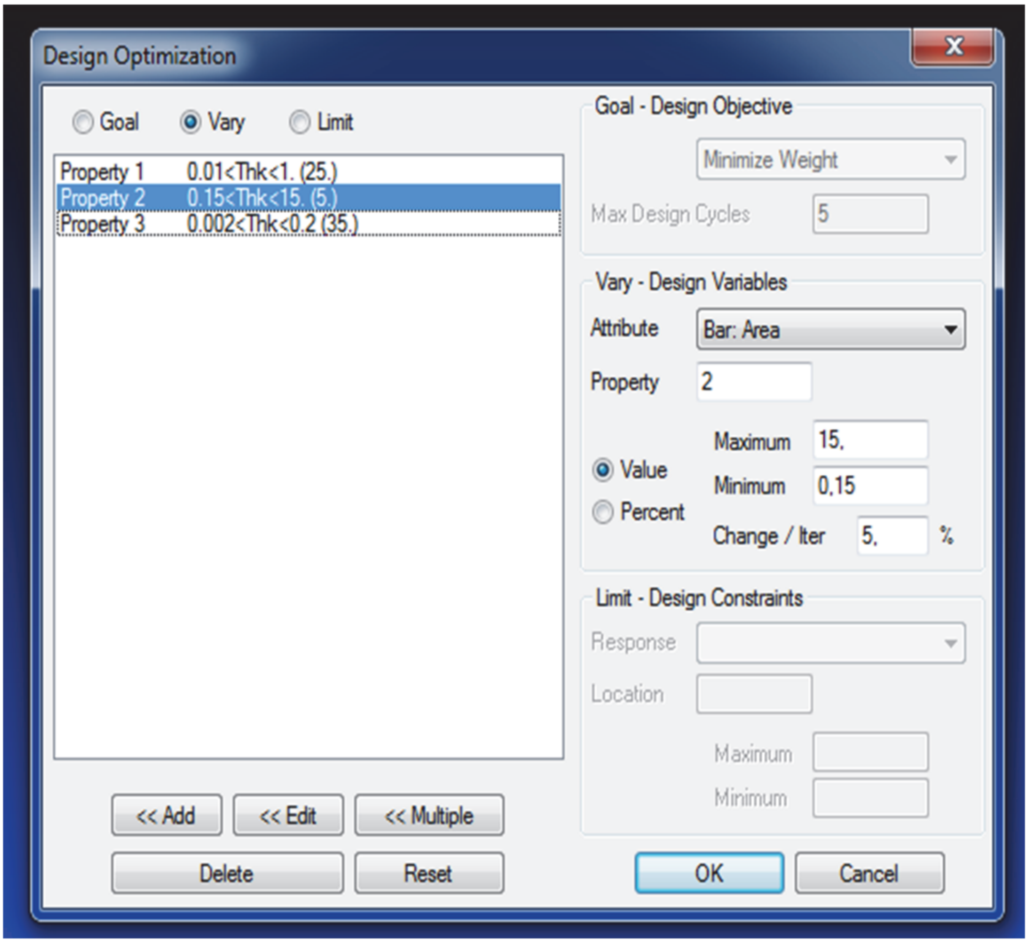

Design Optimization

○ Goal ● Vary ○ Limit

Property 1 0.01<Thk<1. (25.)
Property 2 0.15<Thk<15. (5.)
Property 3 0.002<Thk<0.2 (35.)

Goal - Design Objective

Minimize Weight

Max Design Cycles 5

Vary - Design Variables

Attribute Bar: Area

Property 2

● Value
○ Percent

Maximum 15,
Minimum 0,15
Change / Iter 5, %

Limit - Design Constraints

Figure 43 Command window - Design Variables setup

The last field to be filled is the Limit – Design Constraints. As Response the value not to be exceeded can be found in a drop down list. Settable responses are:

- Node: Displacement (along X, Y or Z direction);
- Node: Rotation (around X, Y or Z axis);
- Rod: Axial or Torsion Stress;

- Rod: Axial or Torsion Strain;
- Bar: Axial Stress;
- Bar: Max or Min Stress;
- Bar: Axial Strain;
- Bar: Max or Min Strain;
- Plate: X or Y Normal Stress;
- Plate: XY Shear Stress;
- Plate: Max or Min Principal Stress;
- Plate: Von Mises Stress;
- Plate: X or Y Normal Strain;
- Plate: XY Shear Strain;
- Plate: Max or Min Principal Strain;
- Plate: Von Mises Strain;

Then the Property ID and the allowable range are to be set.

The results of an optimization analysis are loaded as output files in the Results section of FEMAP's Model Info drop down list. However, this output is just the static analysis ran with the optimum parameters but it is not possible to see the parameters themselves. To do that the .f06 system file has to be open (with any text reader software, here Note Pad ++ is used). There, it can be found the numbers of cycles for the convergence of the solution and the value of the variable at each cycle. Figure 44 and Figure 45 both show the optimization data bulks.

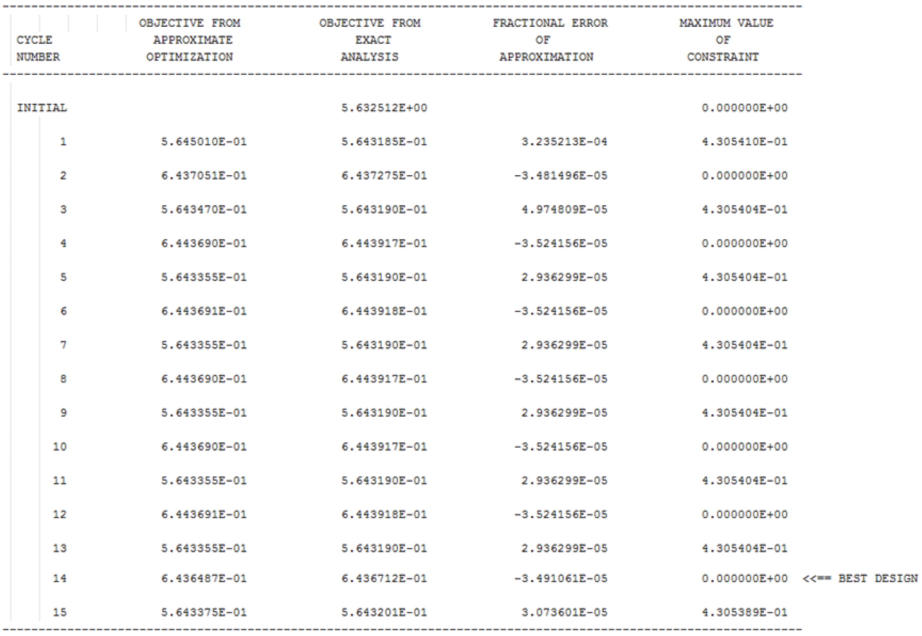

```
-----------------------------------------------------------------------------------------
           OBJECTIVE FROM       OBJECTIVE FROM      FRACTIONAL ERROR      MAXIMUM VALUE
 CYCLE       APPROXIMATE            EXACT                 OF                   OF
 NUMBER      OPTIMIZATION          ANALYSIS          APPROXIMATION         CONSTRAINT
-----------------------------------------------------------------------------------------

 INITIAL                         5.632512E+00                              0.000000E+00

      1      5.645010E-01        5.643185E-01          3.235213E-04        4.305410E-01

      2      6.437051E-01        6.437275E-01         -3.481496E-05        0.000000E+00

      3      5.643470E-01        5.643190E-01          4.974809E-05        4.305404E-01

      4      6.443690E-01        6.443917E-01         -3.524156E-05        0.000000E+00

      5      5.643355E-01        5.643190E-01          2.936299E-05        4.305404E-01

      6      6.443691E-01        6.443918E-01         -3.524156E-05        0.000000E+00

      7      5.643355E-01        5.643190E-01          2.936299E-05        4.305404E-01

      8      6.443690E-01        6.443917E-01         -3.524156E-05        0.000000E+00

      9      5.643355E-01        5.643190E-01          2.936299E-05        4.305404E-01

     10      6.443690E-01        6.443917E-01         -3.524156E-05        0.000000E+00

     11      5.643355E-01        5.643190E-01          2.936299E-05        4.305404E-01

     12      6.443691E-01        6.443918E-01         -3.524156E-05        0.000000E+00

     13      5.643355E-01        5.643190E-01          2.936299E-05        4.305404E-01
     14      6.436487E-01        6.436712E-01         -3.491061E-05        0.000000E+00  <<== BEST DESIGN

     15      5.643375E-01        5.643201E-01          3.073601E-05        4.305389E-01
-----------------------------------------------------------------------------------------
```

Figure 44 Optimization .bdf file

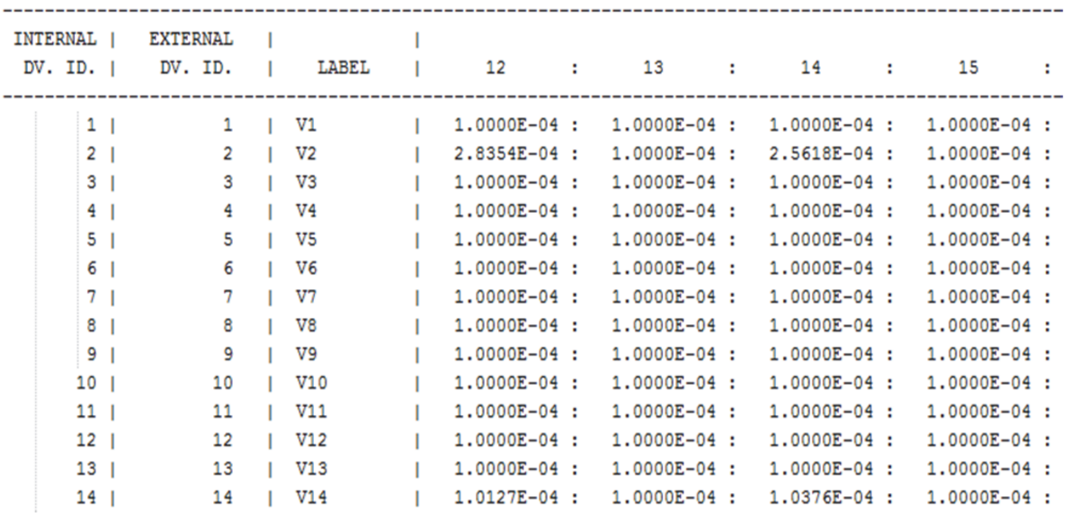

```
-----------------------------------------------------------------------------------------
INTERNAL |  EXTERNAL   |            |
 DV. ID. |   DV. ID.   |   LABEL    |     12      :     13      :     14      :     15      :
-----------------------------------------------------------------------------------------
       1 |           1 | V1         |  1.0000E-04 :  1.0000E-04 :  1.0000E-04 :  1.0000E-04 :
       2 |           2 | V2         |  2.8354E-04 :  1.0000E-04 :  2.5618E-04 :  1.0000E-04 :
       3 |           3 | V3         |  1.0000E-04 :  1.0000E-04 :  1.0000E-04 :  1.0000E-04 :
       4 |           4 | V4         |  1.0000E-04 :  1.0000E-04 :  1.0000E-04 :  1.0000E-04 :
       5 |           5 | V5         |  1.0000E-04 :  1.0000E-04 :  1.0000E-04 :  1.0000E-04 :
       6 |           6 | V6         |  1.0000E-04 :  1.0000E-04 :  1.0000E-04 :  1.0000E-04 :
       7 |           7 | V7         |  1.0000E-04 :  1.0000E-04 :  1.0000E-04 :  1.0000E-04 :
       8 |           8 | V8         |  1.0000E-04 :  1.0000E-04 :  1.0000E-04 :  1.0000E-04 :
       9 |           9 | V9         |  1.0000E-04 :  1.0000E-04 :  1.0000E-04 :  1.0000E-04 :
      10 |          10 | V10        |  1.0000E-04 :  1.0000E-04 :  1.0000E-04 :  1.0000E-04 :
      11 |          11 | V11        |  1.0000E-04 :  1.0000E-04 :  1.0000E-04 :  1.0000E-04 :
      12 |          12 | V12        |  1.0000E-04 :  1.0000E-04 :  1.0000E-04 :  1.0000E-04 :
      13 |          13 | V13        |  1.0000E-04 :  1.0000E-04 :  1.0000E-04 :  1.0000E-04 :
      14 |          14 | V14        |  1.0127E-04 :  1.0000E-04 :  1.0376E-04 :  1.0000E-04 :
```

Figure 45 Optimization .bdf file

An interesting application, present in literature, of NASTRAN's Sol200 is here described. Sol200 has been used to couple FEA (Finite Element Analysis) with a MBS (Multibody System Simulation) in order to obtain the main advantages achievable with both these softwares. Since structural optimization implies a change of the components shape (i.e. the mass distribution) during each iteration, the dynamic inertia loads and the components' dynamical properties change accordingly. In traditional structural optimization, usually constant loads and boundary conditions are used. A coupled MBS-FEA optimization approach opens up the possibility to take these iteration-dependent load changes into account while optimizing the component. This leads to an improved design of the considered component and shorter product development time. Then it was possible to describe the structural optimization of dynamically loaded finite element flexible components embedded in a multibody system by means of an automated coupling of ADAMS as MBS software and Nastran Sol200 as optimizer.

The ADAMS Model consists of a simple crank drive mechanism which dimensions are shown in Figure 46. The multibody system simulates a crankshaft turning with 1500 rpm. Additionally, a force representing a pressure is acting on top of the piston.

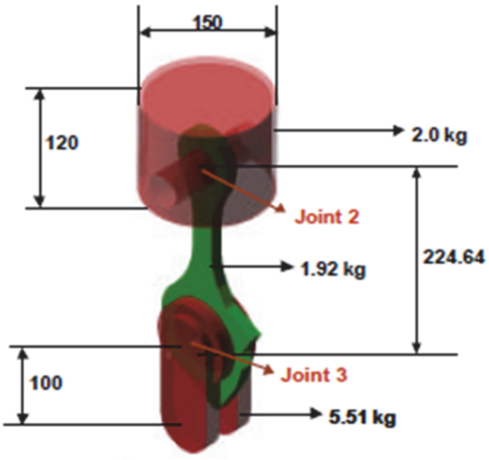

Figure 46 Crank drive

For the modal analysis which is needed for the flexible representation within Adams by means of a component mode synthesis, the nodes of the bearing sets are connected to the centre of rotation of the bearings using RBE2 elements. This means a rigid coupling of all nodes' DOF to the nodes of the centre points.

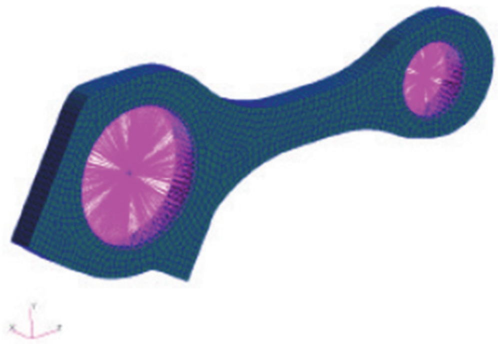

Figure 47 Model of Connecting rod for modal analysis

After the MBS simulation carried out with Adams, the points of time producing the critical loads on the conrod need to be determined. Then the export function of Adams can be used to generate the loads acting on the flexible body in NASTRAN format. These loads can then be used for a static analysis of the body to obtain the stress distribution. The loads exported by Adams are in a dynamic equilibrium, which means that the forces at the supports compensate the inertia forces (however, this is only fulfilled to a certain numerical accuracy). Since there are initially no fixed nodes in the model, something has to be done so that the equilibrium is fulfilled exactly. Without going deep in the description of this problem, the equilibrium was achieved using a method called inertia relief.

In order to change the shape of the rod in the optimization area, pressure loads for surface deformation have been chosen. The Poisson's ratio for this auxiliary analysis has been set to zero so that all the affected nodes make a movement only in the y-z plane. With this shrewdness is possible to generate shape basis vectors for the planned optimization. Each load case is slightly overlapping so that a smooth surface can be formed by the superposition of the shape basis vectors. The mesh is locally adjusted by the movement of the inner nodes caused by the deformation. The objective function for the optimization is the reduction of the weight. As calculation constrain set, a limit on Von Mises stress has been chosen (25 N/mm^2) so that a failure won't occur. Addition constrains (side constrains) were added to limit design variables directly. This means that the maximum "shrinking" is limited to 3 mm and the maximum growth is limited to 40 mm. One reason for this limitation is to keep a reasonable rod design, the other is to control the occurring mesh distortion. There is no GUI for the setup of the approach. The Adams and Nastran models have to be set up as before. Only the parts of the FEM model, which are changed during the optimization, have to be moved to an include-file. These include-files are then accordingly exchanged during the optimization process. There are three necessary include-files:

- <filename>_loads.bdf: Contains the latest loads of the Adams simulation.
- <filename>_optdata.bdf: Contains the updated FEM entries which have been changed by the design variables.
- <filename>_desvars.bdf: Contains the current state of the design variables.

In an individual configuration file amongst some other data the following can be defined:

- Simulation script and load output times of the multibody system simulation.
- Number of maximum internal Sol 200 optimization loops.
- Number of maximum complete optimization loops.

To update the loads is necessary under the following two conditions:

- Large accelerations together with large changes of mass or mass distribution.
- Changes of the mechanical properties of the components which leads to different system behavior.

For the first point, it doesn’t seem to be obvious, why a new multibody simulation is necessary for a load update. The generated Adams acceleration statements should be able to reflect the changes of the components’ mass properties. It is right, that the e.g. reduced mass will produce less inertia forces caused by the accelerations. The problem is, how the above mentioned equilibrium of forces is achieved.

All the proposed methods (listed in the article) to ensure this equilibrium are based on the assumption either that the inertia forces and the support forces are compensating each other. Therefore, additional supports will not change the stress distribution but only produce the minor forces for the exact equilibrium. Or the inertia relief will generate the accelerations necessary for the support forces on the interface nodes. There is no way to generate the support forces necessary to compensate the occurring inertia forces for the scenario shown here. This could only be done if the directions of the support forces could be predicted. Then, support-entries could be used in the FEM model.

Even worse, the inertia relief method will apply higher accelerations to the component, if its mass is reduced to fulfill the equilibrium with the support forces (initially calculated as reaction to the inertia of the larger mass, F=ma= const).

Here, results of the static simulation will be skipped so that a higher focus can be given to optimization results. The shape optimization has been carried out using the Modified Method of Feasible Directions (MMFD) which is the default algorithm for Sol200. The maximum number of iterations has been limited to 30. In addition, the maximum number of constraints to observe has been set to 150 while no other default parameters have been changed. This resulted in an optimization with 30 iterations, stopped aby the maximum number of iterations. The progress of the objective function and the normalized constraint violation can be seen in Figure 48.

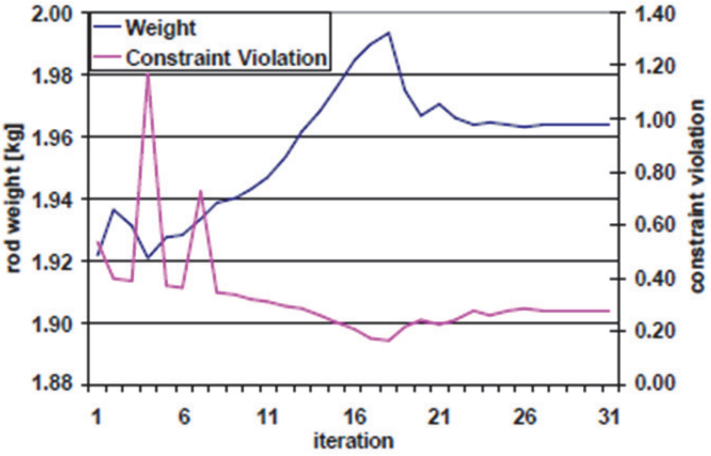

Figure 48 Piston Rod Optimization result

A constraint violation of 0 would indicate no constraint violation, while the final value shows that the model still violates the constraint by about 27%. The authors could not find why the optimizer couldn't find a feasible design since none of the design variables has reached a side constraint. However, the optimization has reached a stress reduction of 26% while gaining only 2% more weight.

Chapter 5 Analysis, Validations and Results

Introduction

In this chapter numerical results of FEMAP analysis will be presented. Validation models will be described as well as the calculus hypothesis under whom formulas are written.

To validate the model, a mass check is performed to make sure no information or geometry is lost during transfers between different softwares and file formats (the geometry is made in FLUENT to calculate aerodynamics loads, exported in SolidWorks to export mean surfaces and passed to FEMAP to be analyzed).

Another preliminary check is made before the static analysis is performed: an extraction of eigenvalues (so that vibrating behavior of the structure is known) by the means of a modal analysis.

To validate static results, the theories of plates and beams are used. A slice of the skin between two consecutive ribs and spar is considered as a simply supported plate with a constant distributed load on its surface. Displacements for both models are confronted with FEMAP results.

Once the validation is performed, different analysis are done to study model's structural behavior and the weight optimization is performed as well. A DOE campaign is set so to understand which parameter (or parameters) have the higher influence.

Figure 49 shows the existing types of structural optimization. Generally, the terms “sizing optimization”, “shape optimization” and “topology optimization” are used for classification. In this work, a sizing optimization is chosen in order to lower the mass.

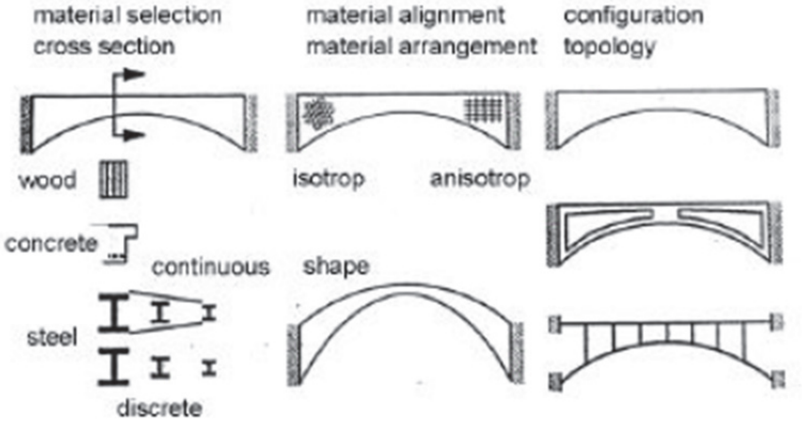

Figure 49 Different types of optimizations

Validating the model.

The first validation step consist in performing a mass check. To perform a mass check it's just necessary to verify the mass output available in each software. Mass output in SolidWorks is quite easy to perform with the solid model. After mean surfaces are extracted, the only information available is the surfaces' area so that it has to be multiplied by thickness x density to obtain its mass. Mass output in FEMAP can be performed following two different ways: a geometric check and a mesh check. Geometric check gives geometry's volume as output and multiplies by a given density. Mesh check is available after a complete mesh is ready, it gives the mass according with defined Properties. Mass output in FLUENT is given by previous checks. Since all the values are almost the same it can be stated that no information is lost during transfers.

The second check is done by the means of a modal analysis. This is to verify that the first eigenvalue obtained by FEMAP has a correct physical meaning. The boundary condition given to the model is a clamp on spars and on skin's curve closer to the fuselage (see Figure 50). To write a validating equation the following hypothesis are needed.

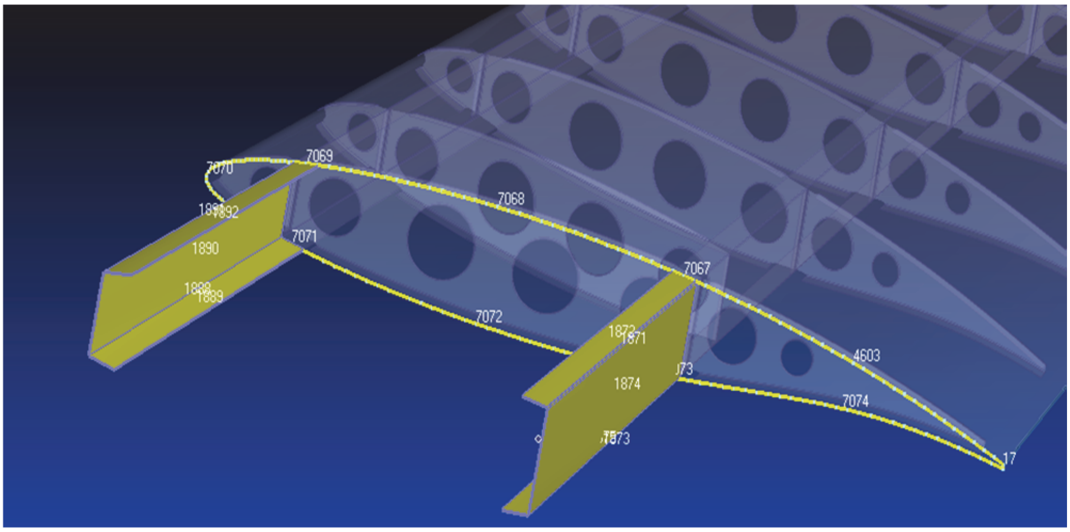

Figure 50 Bonds' Positions

The wing is approximate as a clamped beam with a regular cross section; this assumption is usually done to study wings and it's not a strong one. Once these simplifications are done, the well known equations for cantilever beams can be used. The following equation is used to obtain the first eigenvalue:

$$\omega_1 = \beta_1^2 \sqrt{\frac{EI}{m}}$$

With $\beta_1 L=1.8751$. E is the Young's modulus, I the second moment of inertia, m the mass per unit of length and L the spanwise length.

The cross section of the beam is chosen as the combination of two C-shaped beams and an elliptical profile. This simplified geometry is symmetric to the x axis and can be easily evaluated (see Figure 51, the black curve is the original shape, the blue one is the ellipse).

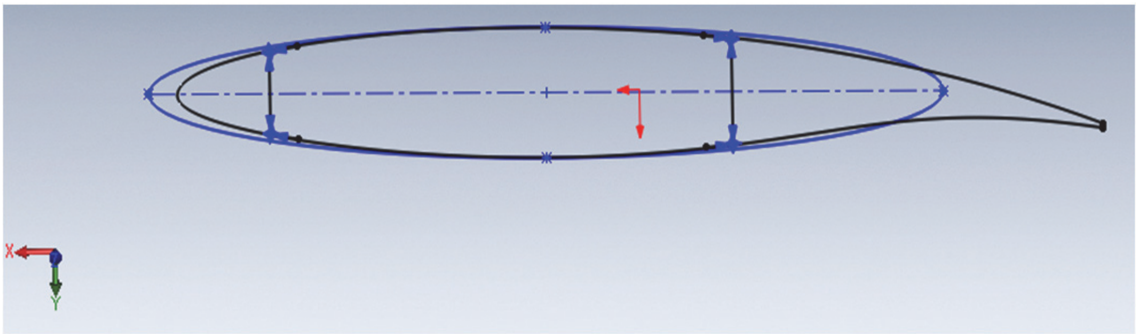

Figure 51 Beam's Cross Section approximation

Once the cross section is defined, three different scale length are used. This is because wing's cross section becomes smaller and smaller along the spanwise direction. The considered sections are the ones corresponding to the fixed end (biggest one), to the free end (smallest one) and at the center. The biggest section is approximately three times bigger than the smallest one, so a multiplier of 2 is chosen to represent the section at the middle. Values and equations are listed below (if not stated otherwise, values reported in the table are mm; the whole geometry is considered to be thin with a thickness t=0.5mm).

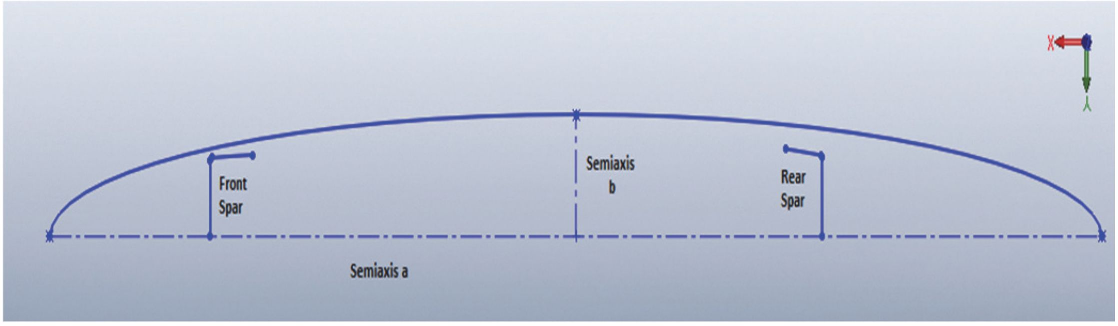

Figure 52 Nomenclature of the Geometry

$$I_{x,Tot} = I_{x,Front\ Spar} + I_{x,Rear\ Spar} + I_{x,Ellipse}$$

Table 6

		Section Scale			FEMAP Solution
		Small (1x)	Medium (2x)	Big (3x)	
Front Spar	Web	8.7	17.4	26	
	Flange	6.7	13.4	20	
Rear	Web	11	22	33	

Spar	Flange	6.7	13.4	20	
Ellipse's Semiaxis	a	93.5	187	280.45	
	b	13.8	27.6	41.4	
I_x [m^4]		25.482 10^{-9}	0.204 10^{-6}	0.686 10^{-6}	
First Eigenvalue [Hz]		6.9	19.3	33.1	30.1

The results presented in the table shows a good agreement between the simplified model and FEMAP calculation.

As further validation procedure, a static analysis is performed in FEMAP and the results are compared with the typical solution of a cantilever beam of constant section. The well-known solution for the displacement of a cantilever beam is:

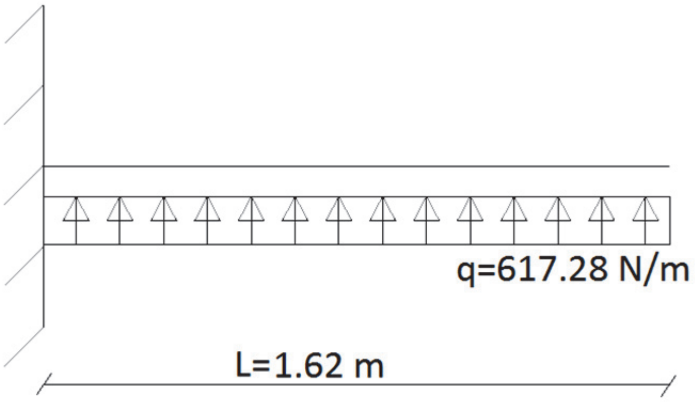

Figure 53 Beam Approximation: Load and Length

$$\frac{d^2v}{dx^2} = -\frac{M}{EI}\;;$$

$$\frac{dv}{dx} = \varphi = -\frac{q}{2EI}\left(\frac{x^3}{3} - Lx^2 + L^2x\right) + C_1\;;$$

$$v = -\frac{q}{2EI}\left(\frac{x^4}{12} - \frac{Lx^3}{3} + \frac{L^2x^2}{2}\right) + C_1x + C_2\;;$$

Where the constants C_1 and C_2 are found with the border conditions:

$$\varphi(x = 0) = 0\,;$$

$$v(x = 0) = 0\,;$$

These border conditions yield to:

$$C_1 = C_2 = 0\,;$$

The distributed load is found from the total lift (1000 N) divided for the length of the beam (1.62 m). Value for I is the same found in the modal analysis above discussed and E is aluminum Young's modulus. Results of this comparison are shown in Table:

Table 7

Cantilever Beam Validation		
	FEMAP	Analytical
Displacement Max [mm]	15.2	11.1

The last validating step is a control of the displacement coming from the thin plate theory. A slice of the skin among two consecutive ribs and the spars has been selected (so that a "plate" is obtained). The selected plate is located at the end of the wing (in the spanwise direction) so that its shape is as close as possible similar to a square. The displacement of this part of the skin is composed by two contributions: the one due to the deformation of the wing and the one due to the pressure load itself. In order to confront FEMAP's result with the analytical one it has to be purged of the contribution coming from the interaction with the rest of the wing. The average displacement of the points shown in Figure 54 are considered to be representative of this contribution. The equation used to evaluate the displacement due to the pressure is (the value to be compared is the maximum one, located at the center of the plate):

$$w(x,y) = \frac{16\,p}{\pi^6 D}\sum_{m=1,3,5}^{\infty}\sum_{n=1,3,5}^{\infty}\frac{\sin\frac{m\pi x}{L_x}\,\sin\frac{n\pi y}{L_y}}{mn[\left(\frac{m}{L_x}\right)^2+\left(\frac{n}{L_y}\right)^2]^2}\,;$$

Where

$$D = \frac{E\,t^3}{12(1-\nu^2)}\ ;$$

Represents plate's stiffness and

$$W_{max} = W\left(\frac{L_x}{2}, \frac{L_y}{2}\right)\ ;$$

The above displacement is based on the first 4 x 4 = 16 terms of the series solution. The constant value of the pressure has been evaluated by a mean of the pressures acting in this zone. The other values used to evaluate the displacement are reported in the table below:

Table 8

Calculus values	
L_x	0.156 m
L_y	0.161 m
P	1000 Pa
t	1.1 mm
E	70 GPa
ν	0.34
D	8.779 Pa m^3

Table 9

Plate Theory validation		
	FEMAP	Equation
Displacement Max [mm]	0.11	0.23

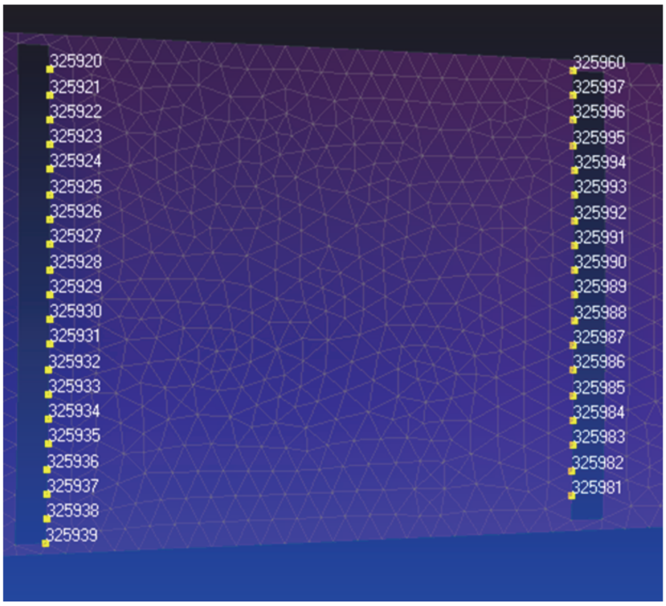

Figure 54 Points used to evaluate plate's average displacement

Analysis

The next step is to perform the static analysis of WT model. Constraint conditions are the same as for preliminary analysis (a clamp on spars and on skin's curve closer to the fuselage) so to represent the WT test conditions.

First of all, all the thicknesses are set to 0.5 mm and the analysis is launched. The results are shown below:

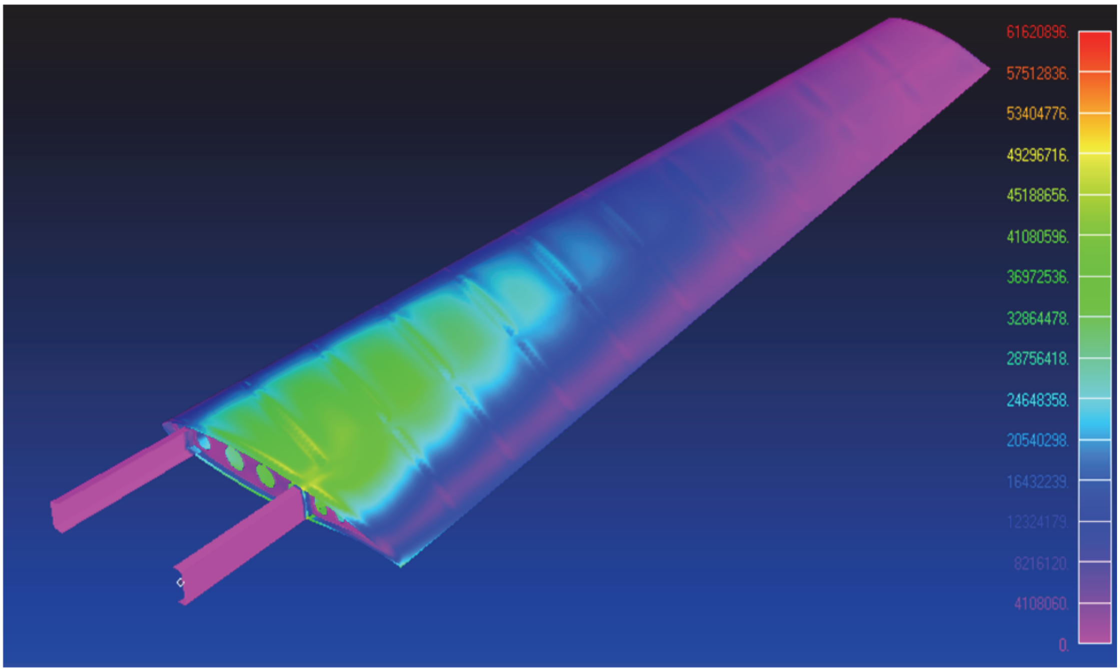

Figure 55 Static Analysis' result

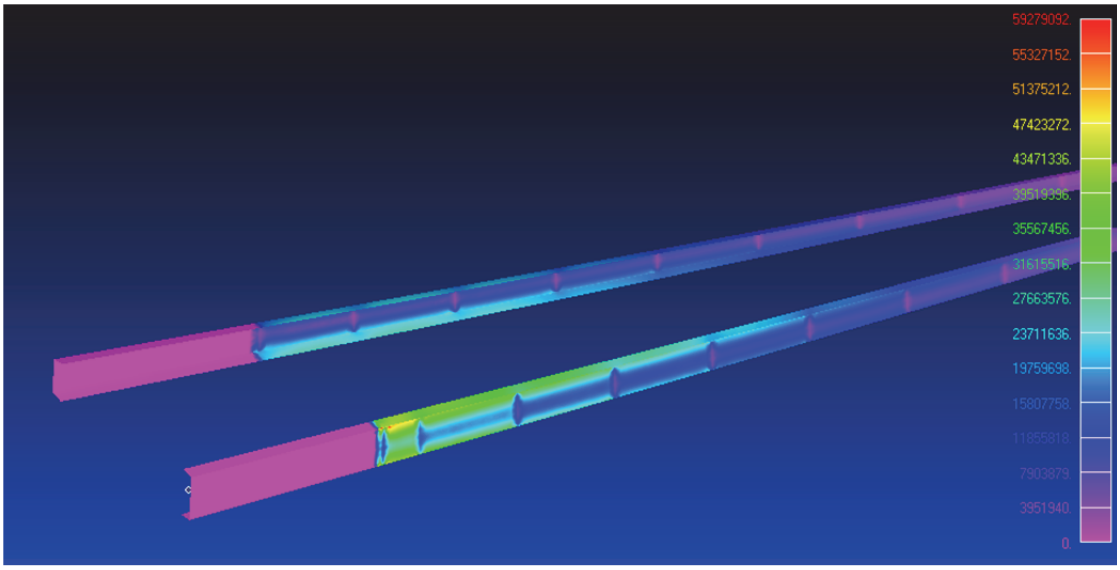

Figure 56 Static Analysis result of the Spars

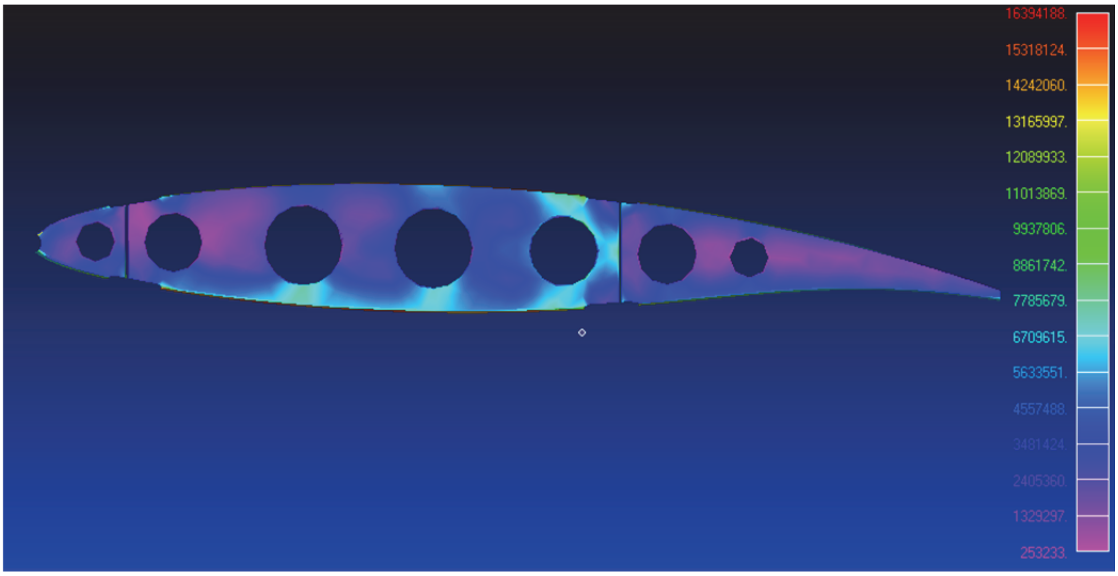

Figure 57 Static Analysis result of a Rib

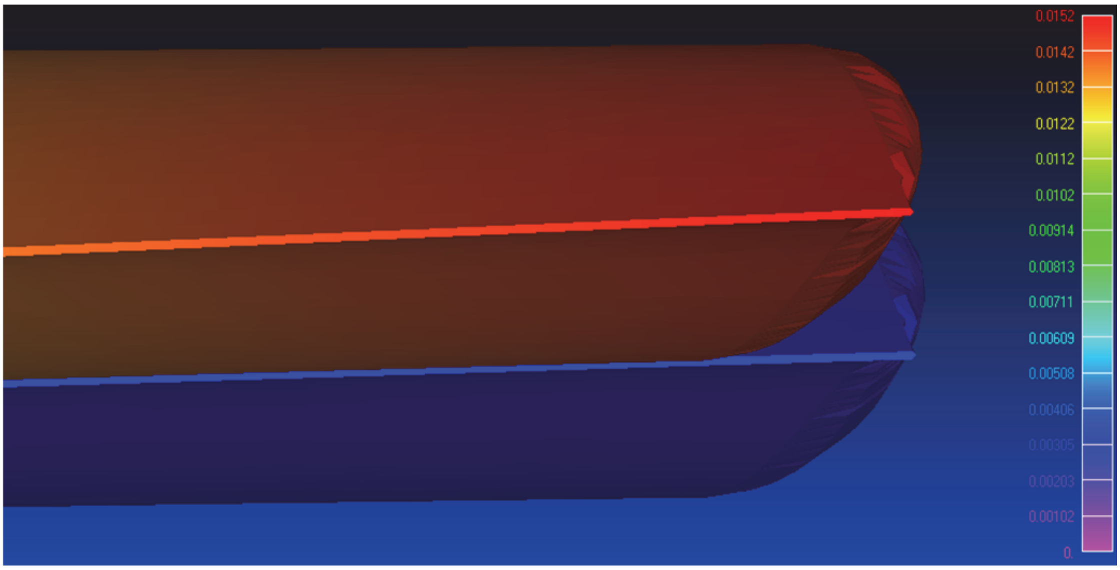

Figure 58 Maximum Displacement (wing tip)

In Figure 55 the overall stress distribution is presented. The maximum Von Mises tension results to be close to the fixed edge with a value of 61.6 MPa. Figure 56 shows spars' behavior: the rear one is designed to withstand more load than the front one so that, with the same thickness, it reaches higher tension level; this behavior is clearly confirmed from the analysis, values of top stresses are ca. 45 MPa for the rear spar and ca. 16 MPa for the front one. Figure 57 shows ribs behavior: they aren't designed to sustain a high level of load (which is demanded to the spars) so that the maximum stress value is approximately of 5 MPa. Lastly

Figure 58 shows the maximum displacement: its value is 15.2 mm and it's located at the wing tip.

The results here presented are for static analysis with a first attempt set of thicknesses. Several considerations can be made at this point: because of the above mentioned motivations, ribs' and skin thicknesses can be lowered and, meanwhile, spars' thicknesses must be increased. Regarding the skin, it is important to note that the structure is subject to compressive loads, so a buckling analysis is mandatory.

Using buckling analysis results, it can be noted that the structure fails because of second order deformation (Figure 59). Because of this, skin's thickness must be increased to avoid the failure. The failure at that very zone happens because there is an incomplete rib, as shown in the Figure 60.

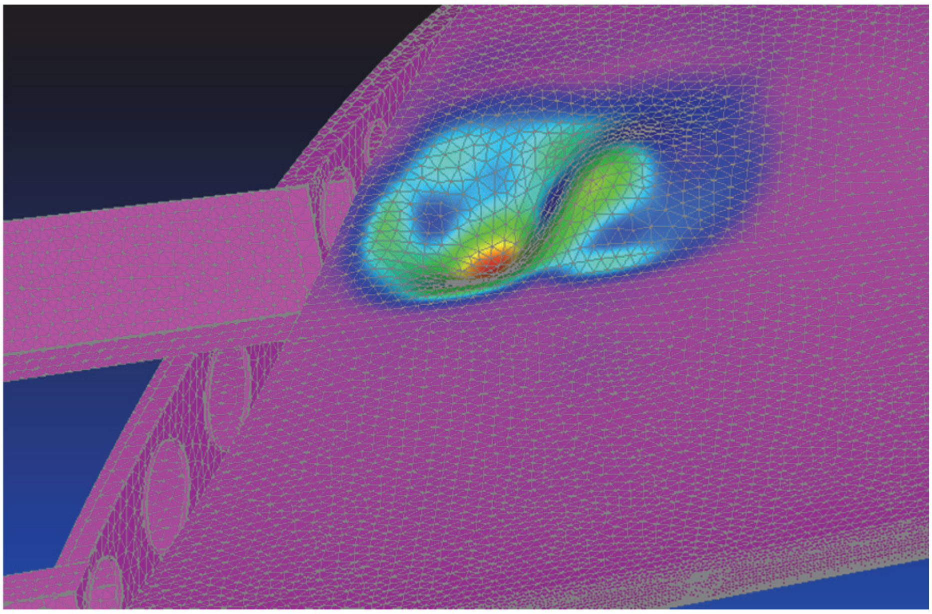

Figure 59 Buckling Zone

Figure 60 Buckling Zone corresponding to a rib's missing tail

With this results as baseline, an optimization analysis is run. The results are listed in the table below:

Table 10

Optimization results (thicknesses [m])	
Front Spar	1.0000E-04
Rear Spar	2.5618E-04
Rib 1	1.0000E-04
Rib 2	1.0000E-04
Rib 3	1.0000E-04
Rib 4	1.0000E-04
Rib 5	1.0000E-04
Rib 6	1.0000E-04
Rib 7	1.0000E-04
Rib 8	1.0000E-04
Rib 9	1.0000E-04
Rib 10	1.0000E-04
Rib 11	1.0000E-04
Skin	1.0376E-04

With these results a buckling analysis is done but they are found to be inadequate to ensure buckling resistance. After several attempts, the following values were found so that the structure needs a load 46,0% higher than the applied one to fail.

Table 11

Second attempt thicknesses [m]	
Front Spar	1.0000E-03
Rear Spar	1.5000E-03
Rib 1	3.0000E-04
Rib 2	3.0000E-04
Rib 3	3.0000E-04
Rib 4	3.0000E-04
Rib 5	3.0000E-04
Rib 6	3.0000E-04
Rib 7	3.0000E-04
Rib 8	3.0000E-04
Rib 9	3.0000E-04
Rib 10	3.0000E-04
Rib 11	3.0000E-04
Skin	8.0000E-04

Here it is showed the failing zone with the second thicknesses set (Figure 61).

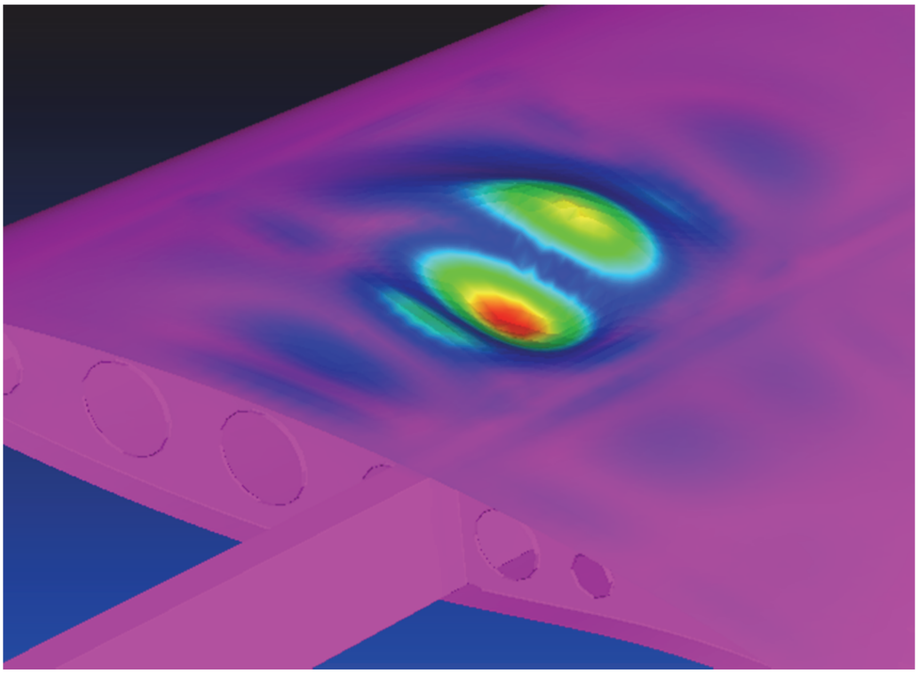

Figure 61 Buckling Zone after first optimization

Even if using this set of values the structure won't fail under the applied pressure, some considerations are to be done. First of all, a value of 0.3 mm as thickness was found to be too small for a structural element. As second matter, the value of 1.46 as buckling safety factor has to be increased to 3 so to take into account possible load oscillations.

To find out in which way thicknesses are to be changed in order to reach an higher safety factor a DOE (Design Of Experiment) campaign is set.

First of all, 19 design points are created using a pseudo-random procedure; each DP is a complete set of the 14 thicknesses (the variation range is defined from 0.5 mm up to 1.5 mm). In Table 12 the DP are shown.

Table 12

	Design Points			
	DP1	DP2	DP3	DP4
Front Spar	0.625	1.075	0.975	1.225
Rear Spar	1.125	1.275	1.475	0.725

Rib 1	1.375	0.575	1.425	0.725
Rib 2	1.375	0.825	0.575	0.675
Rib 3	0.675	0.925	1.225	1.475
Rib 4	0.625	1.375	0.925	1.175
Rib 5	0.575	0.975	0.875	1.475
Rib 6	1.325	1.425	0.575	1.025
Rib 7	0.775	0.575	0.925	1.475
Rib 8	0.875	0.975	1.175	0.925
Rib 9	0.875	1.275	0.775	0.925
Rib 10	0.675	0.575	0.725	1.175
Rib 11	0.875	1.325	1.275	1.125
Skin	0.925	1.025	1.275	1.325

	Design Points				
	DP5	DP6	DP7	DP8	DP9
Front Spar	0.675	0.825	0.725	0.775	1.175
Rear Spar	1.025	0.625	0.775	1.375	1.225
Rib 1	1.125	0.525	0.925	0.675	1.075
Rib 2	0.525	1.125	1.475	1.175	1.025
Rib 3	0.625	0.525	1.375	0.575	0.775
Rib 4	0.975	1.275	1.075	0.825	1.325
Rib 5	0.775	1.075	0.825	1.425	0.925
Rib 6	1.275	1.125	0.675	0.625	0.525
Rib 7	1.425	1.175	0.975	1.025	0.675
Rib 8	1.025	1.375	1.075	0.575	1.275
Rib 9	1.225	0.625	1.475	1.175	1.325
Rib 10	1.275	0.975	0.775	1.125	1.425
Rib 11	1.425	0.675	0.925	1.225	0.775
Skin	0.875	1.075	1.475	1.175	0.575

	Design Points				
	DP10	DP11	DP12	DP13	DP14
Front Spar	1.475	1.275	1.425	1.125	0.525
Rear Spar	1.075	0.675	1.325	0.925	0.875
Rib 1	0.975	1.025	1.225	1.175	1.275
Rib 2	0.875	1.225	1.425	1.275	1.325
Rib 3	0.725	1.175	1.125	0.975	1.275
Rib 4	0.875	0.725	1.225	1.475	0.675
Rib 5	0.525	1.125	1.025	0.725	1.225
Rib 6	0.875	1.375	1.475	0.975	0.825
Rib 7	1.375	0.875	1.325	0.825	1.275
Rib 8	0.725	0.525	1.475	0.775	1.325
Rib 9	1.025	1.425	1.075	0.575	0.725
Rib 10	1.075	1.325	0.925	1.475	1.375
Rib 11	0.575	1.025	1.075	1.475	1.175
Skin	1.425	0.675	0.975	1.225	0.775

	Design Points				
	DP15	DP16	DP17	DP18	DP19
Front Spar	0.925	1.325	1.375	0.875	0.575
Rear Spar	1.175	0.575	0.825	0.525	0.975
Rib 1	0.825	0.625	1.325	1.475	0.875
Rib 2	0.725	0.925	1.075	0.625	0.775
Rib 3	1.025	1.075	0.875	0.825	1.425
Rib 4	0.525	0.575	1.125	1.025	1.425
Rib 5	1.325	0.675	1.375	1.275	0.625
Rib 6	1.075	0.725	0.775	1.175	0.925
Rib 7	1.225	0.725	1.075	0.525	1.125
Rib 8	1.425	1.225	0.625	1.125	0.675
Rib 9	1.375	0.825	0.675	1.125	0.975
Rib 10	0.625	0.825	0.525	1.025	0.875

Rib 11	0.625	1.375	0.975	0.825	0.725
Skin	0.725	0.825	0.625	1.375	0.525

In order to analyze all the DP an automated procedure is performed. This is possible in FEMAP using its Application Programming Interface (API). The API allows to compile a personalized routine and to have it running on a FEMAP model. The routine is written in Visual Basic using dedicated libraries. The routine is divided in two different programs: the first one (Startloop) reads the DPs and does the first analysis (DP1), the second part of the program (Callback) continues the analysis and stops the loop after the last DP. Here is presented the code of the routine.

- Startloop:

```
Sub Main
        Dim App As femap.model
  Set App = feFemap()
        Dim pr As femap.Prop
        Set pr = App.feProp
        Dim pset As femap.Set
        Dim Var As femap.Var
        Set Var = App.feVar
        Dim thickness (14)  as Double
        Dim i as Integer
        Dim readFile As femap.Read
  Set readFile = App.feRead
  Dim s As String
        s = MacroDir + "\tabella thick.txt"
  rc2 = readFile.Open(s, 260)
        If rc2 = FE_OK Then
                rc2 = readFile.Read
                        For i = 0 To 13
                        thickness(i)= readFile.RealField( i+1, 50.0 )
                        MsgBox( str(thickness(i)))
                next
                pos = readFile.Position()
                rc2 = readFile.Open( "tabella thick.txt", 260 )
        Else
                MsgBox( "Unable to open text file",vbOkOnly)
        End If
        rc = Var.Define ("POS", Str(pos))
  Dim path As String
  path = MacroDir + "\callback5.bas"
        App.Pref_OutputSetTitles = 1
        rc = App.feAppEventCallback (FEVENT_RESULTSEND,path )
```

```
            Dim aset As femap.AnalysisMgr
            Set aset = App.feAnalysisMgr
            If Not readFile.AtEOF Then
                        For i = 0 to 13
                                    pr.Get(i+1)
                                    pr.pval(0) = thickness(i)
                                    pr.Put(i+1)
                        next
            aset.Get (3)
            aset.title()  = "Analysis" + Str(thickness(1))
            aset.Put(3)
            aset.Analyze (3)
            Else
            App.feAppEventCallback (FEVENT_RESULTSEND, "")
            End If
End Sub
```

- Callback:

```
Sub Main
            Dim App As femap.model
   Set App = feFemap()
            Dim V As femap.Var
            Set V = App.feVar
            Dim pr As femap.Prop
            Set pr = App.feProp
            Dim aset As femap.AnalysisMgr
            Set aset = App.feAnalysisMgr
            Dim readFile As femap.Read
   Set readFile = App.feRead
            Dim thickness (14)  as Double
            Dim pos as integer
            p = V.GetVarID ("POS")
            rc = V.Get(p)
            pos = V.value
            Dim s As String
            s = MacroDir + "\tabella thick.txt"
   rc2 = readFile.Open( s, 260 )
            If rc2 = FE_OK Then
                        readFile.Jump(pos)
                                    If readFile.AtEOF Then
                                                msgbox("EOF")
                                                App.feAppEventCallback (FEVENT_RESULTSEND, "")
                                                exit sub
                                    end if
                                    rc2 = readFile.Read()
                                    For i = 0 To 13
                                    thickness(i)= readFile.RealField( i+1, 0.0 )
                                    'MsgBox( str(thickness(i)))
                        next
```

```
            pos = readFile.Position()
            V.value = pos
            V.Put(p)
            rc2 = readFile.Open( "tabella thick.txt", 260 )
    Else
        MsgBox( "Unable to open text file",vbOkOnly)
        exit sub
    End If
        For i = 0 to 13
            pr.Get(i+1)
            pr.pval(0) = thickness(i)
            pr.Put(i+1)
        next
        aset.Get (3)
        aset.title()  = "Analisys" + Str(thickness(1))
        aset.Put(3)
        aset.Analyze (3)
End Sub
```

Once the outputs are ready, a post processing is performed to have a further comprehension of parameters' influence on the problem. As goal parameters, buckling safety factor and total mass are chosen. Reading Figure 62 is clear that a better safety factor is achieved by increasing the mass.

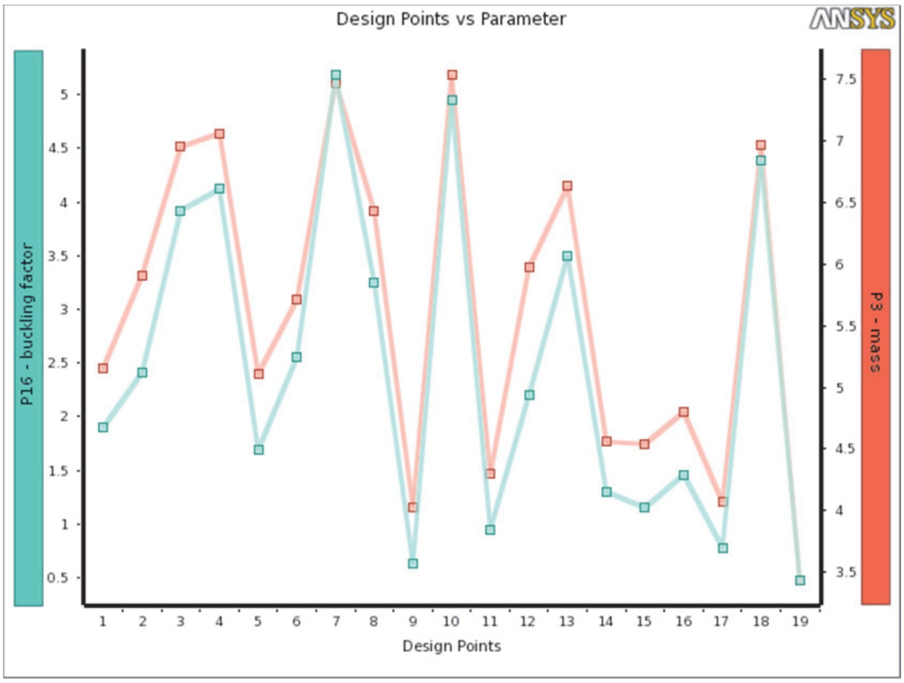

Figure 62 Design Points vs Parameter

Between these parameters, the most important ones are found plotting the Sensitivity Bar (Figure 63) and Sensitivity Pie (Figure 64).

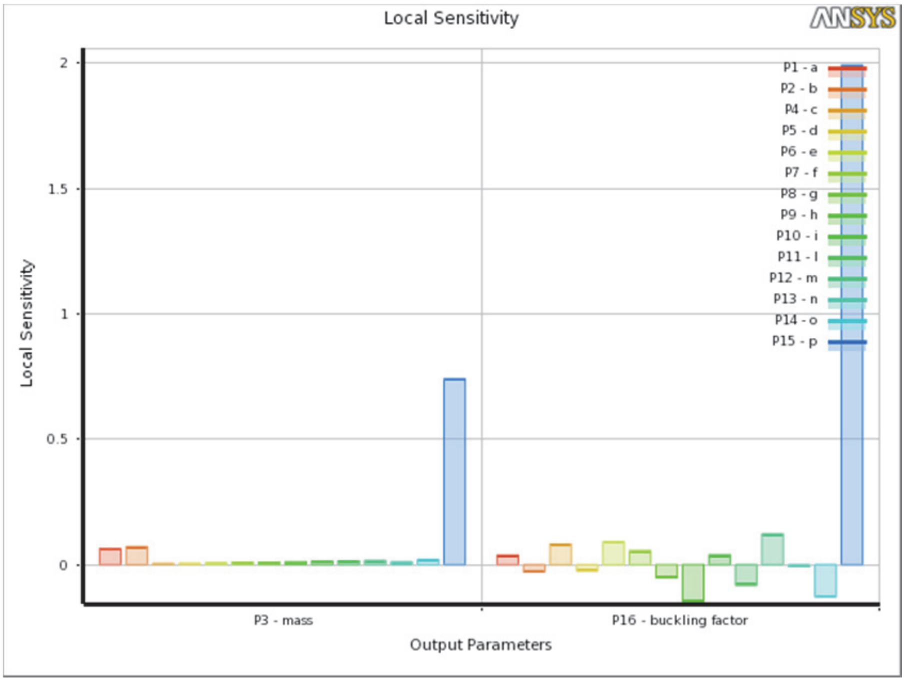

Figure 63 Sensitivity Bar

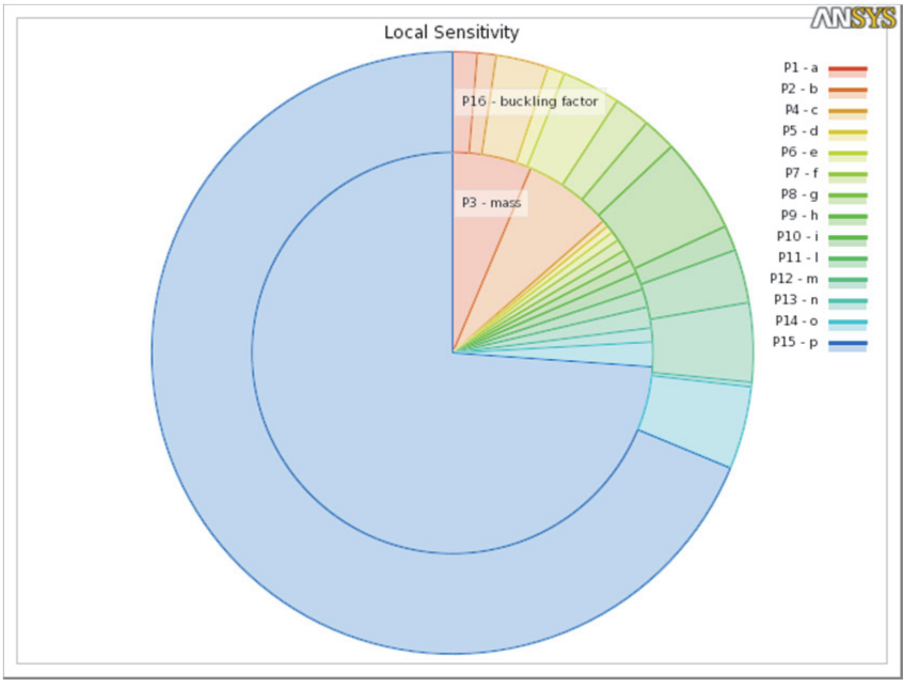

Figure 64 Sensitivity Pie

This behavior is confirmed also by plots in the following Figures.

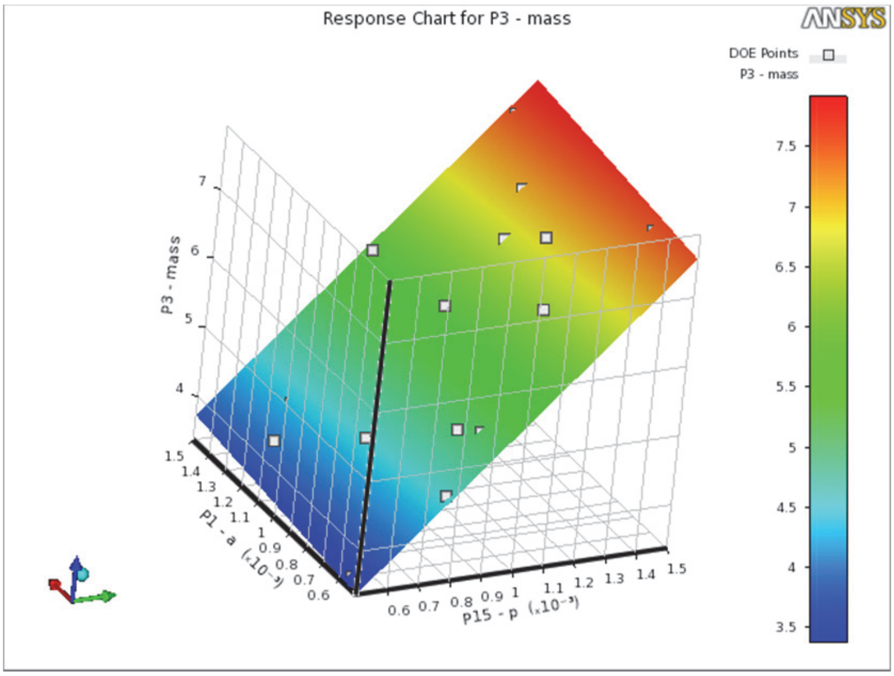

Figure 65 Rear Spar (y-axis) and Skin (x-axis) thicknesses vs Mass (z-axis)

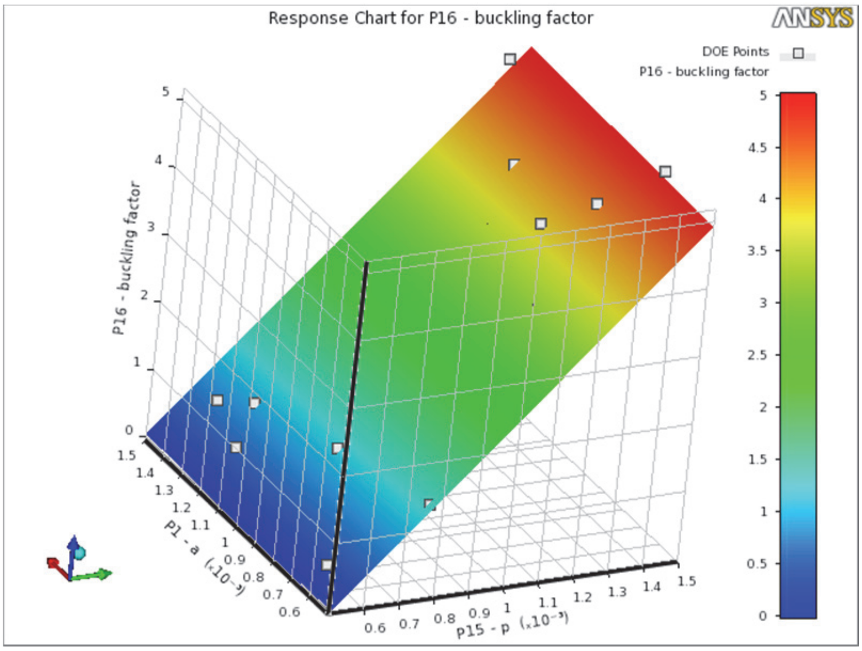

Figure 66 Rear Spar (y-axis) and Skin (x-axis) thicknesses vs Buckling Factor (z-axis)

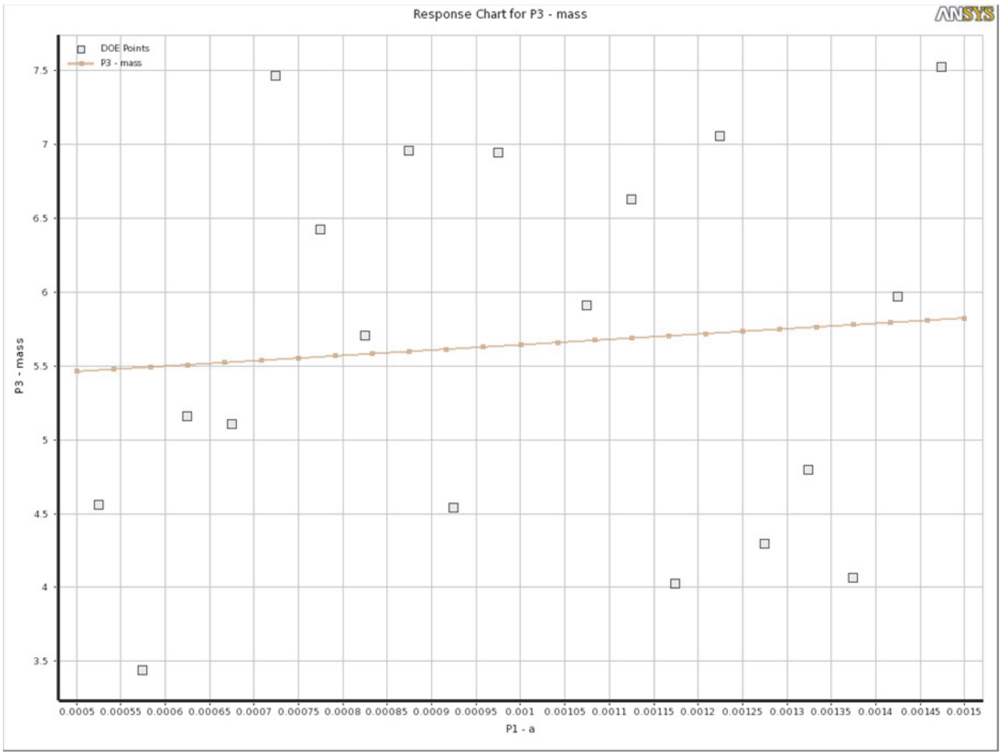

Figure 67 Rear Spar's thickness vs mass

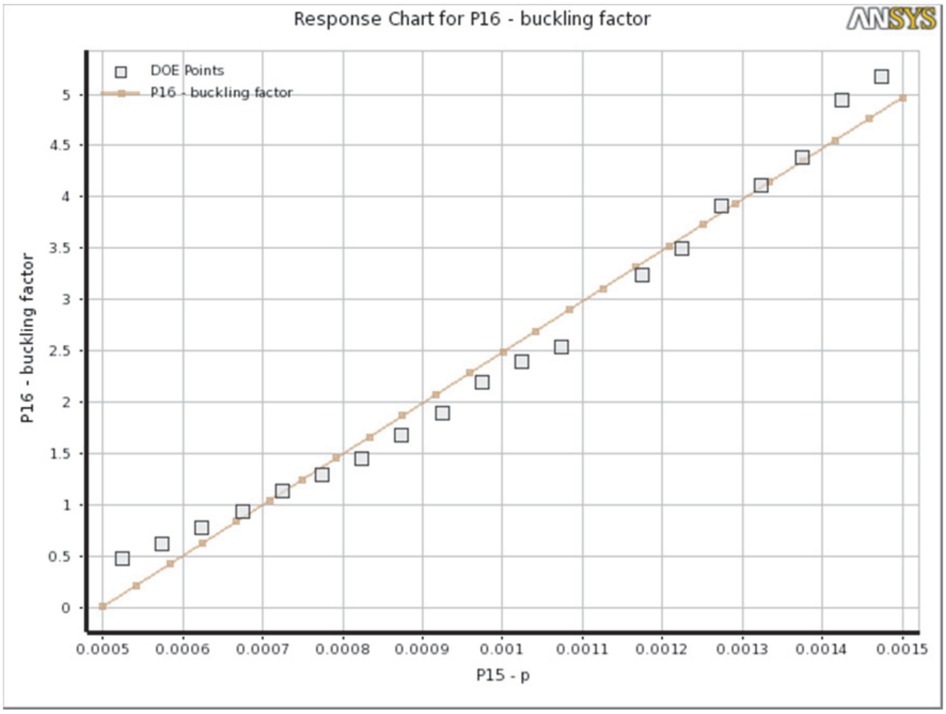

Figure 68 Skin's thickness vs buckling factor

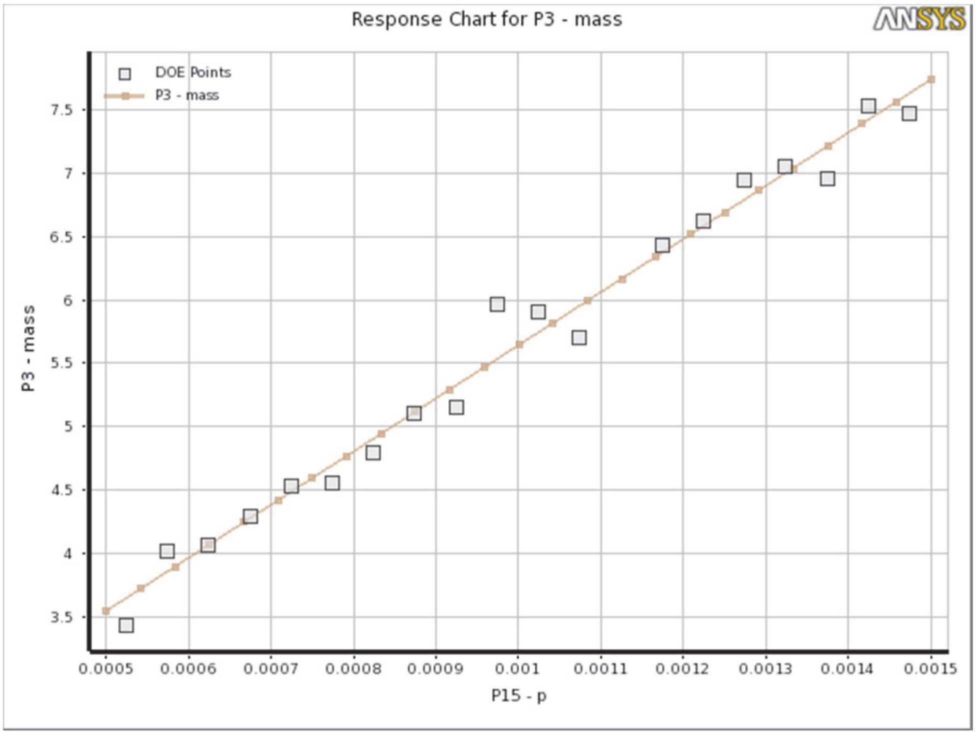

Figure 69 Skin's thickness vs mass

Using this post processing, it is clear that the better way to increase the buckling factor is to act on the skin.

In Table 13 the design thickness set are shown:

Table 13

Final thicknesses set [m]	
Front Spar	1.0000E-03
Rear Spar	2.0000E-03
Rib 1	5.0000E-04
Rib 2	5.0000E-04
Rib 3	5.0000E-04
Rib 4	5.0000E-04
Rib 5	5.0000E-04
Rib 6	5.0000E-04
Rib 7	5.0000E-04
Rib 8	5.0000E-04
Rib 9	5.0000E-04

Rib 10	5.0000E-04
Rib 11	5.0000E-04
Skin	1.1000E-03

In Table 14 the results of first and last analysis are compared.

Table 14

Comparison between Results				
	Max Displacement	Max Von Mises Stress	Safety Factor	Total Mass
First set	15.2 mm	61.62 MPa	0.41	2.81 Kg
Last set	6.67 mm	28.12 MPa	2.92	6.12 Kg
Difference	-56.1%	-54.3%	+612.2%	+117.8%

As clear from these datas, the most important feature reached is the increased Safety Factor: it is very important that no failure occurs while the model is being tested to prevent damages to the wind tunnel, operators and the model itself. There isn't any particular constraint concerning displacements. About maximum stresses, it is mandatory to remain in the elastic field; even if the aluminium alloy to be used has not been chosen yet it is evident, looking at the stresses in Table 14, that any alloy can withstand this amount of load. The total mass increases a lot as percentage value, but it is clear that a model of 6.12 Kg is as easy to handle as a model of 2.81 Kg. Further considerations about the weight have to be done once the material supplier and the model builder are chosen.

Normal modes are shown in the following figures (from Figure 70 to Figure 79, with the modes showed in Figure 77 and Figure 79 referring to ribs) and with their values listed in the table below. Only the first 10 modes were extracted because they fully represent wing's deformation.

Table 15

Normal modes	
1st mode	31.58943 Hz
2nd mode	128.5611 Hz
3rd mode	188.992 Hz
4th mode	195.3383 Hz
5th mode	273.947 Hz
6th mode	311.978 Hz
7th mode	344.0637 Hz
8th mode	354.2327 Hz
9th mode	365.3801 Hz
10th mode	370.3842 Hz

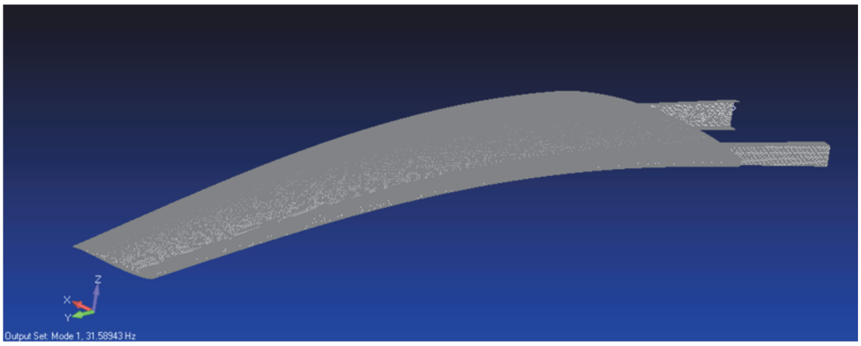

Figure 70 1st mode: 31.58943 Hz

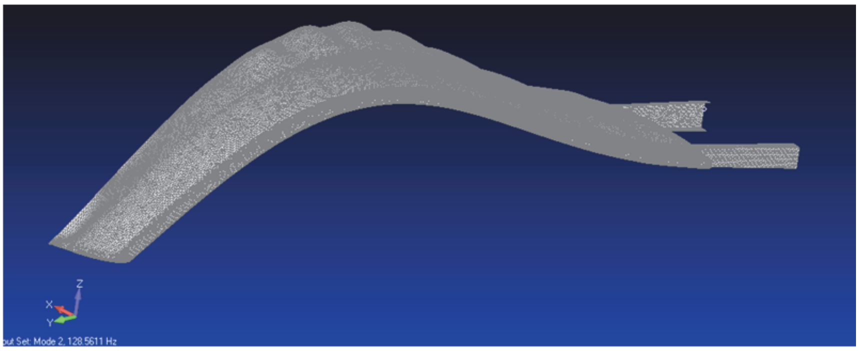

Figure 71 2nd mode: 128.5611 Hz

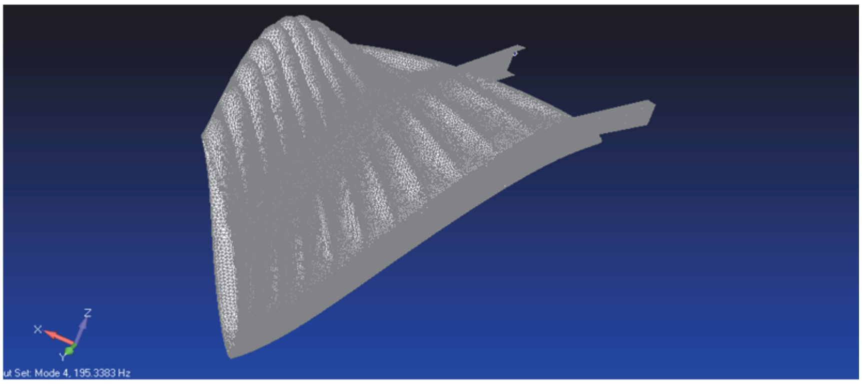

Figure 72 3rd mode: 188.992 Hz

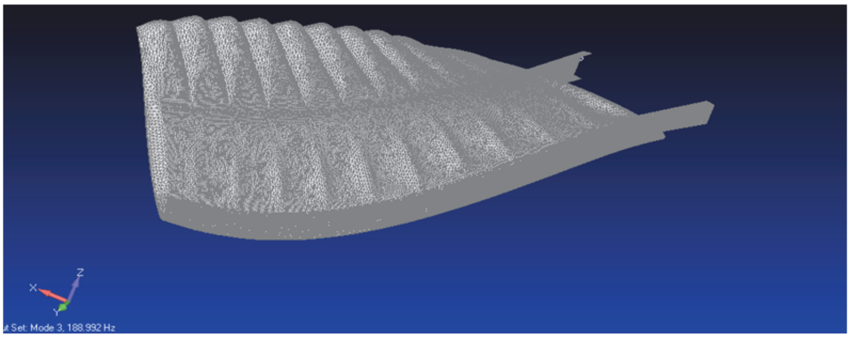

Figure 73 4th mode: 195.3383 Hz

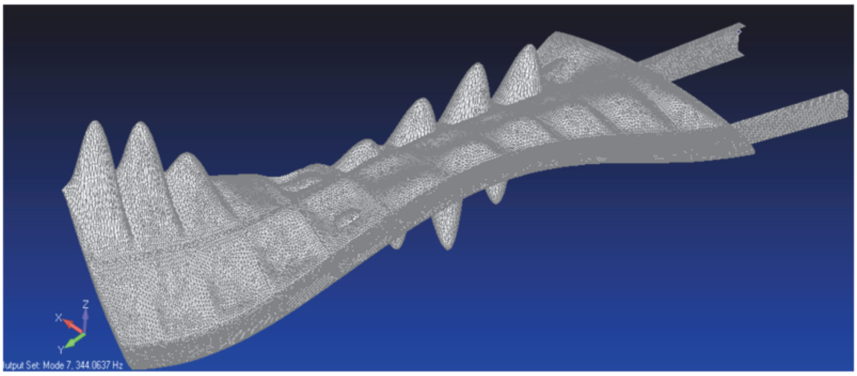

Figure 74 5th mode: 273.947 Hz

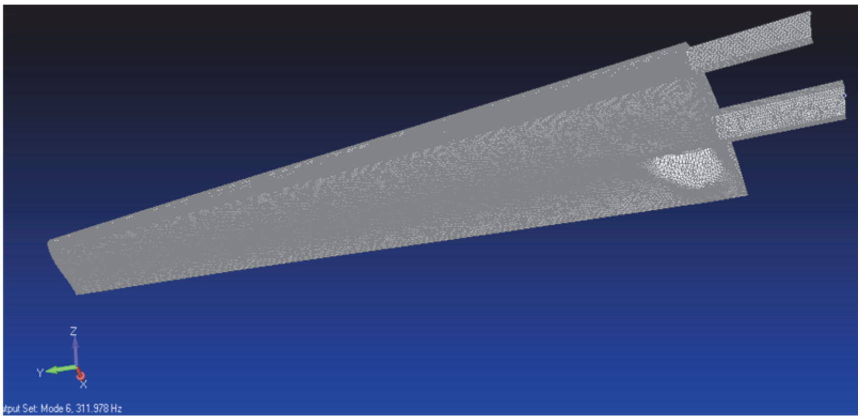

Figure 75 6th mode: 311.978 Hz

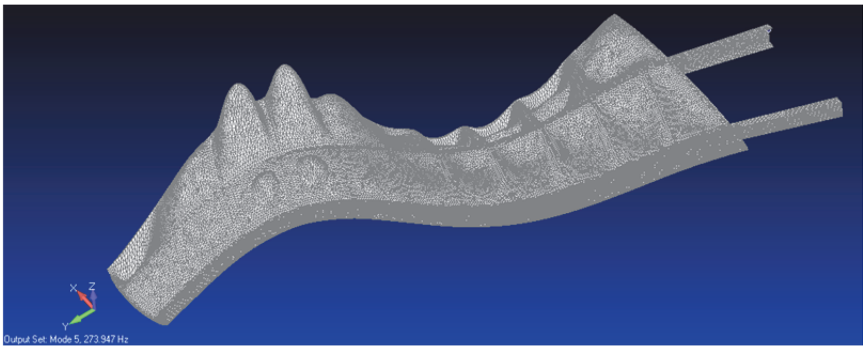

Figure 76 7th mode: 344.0637 Hz

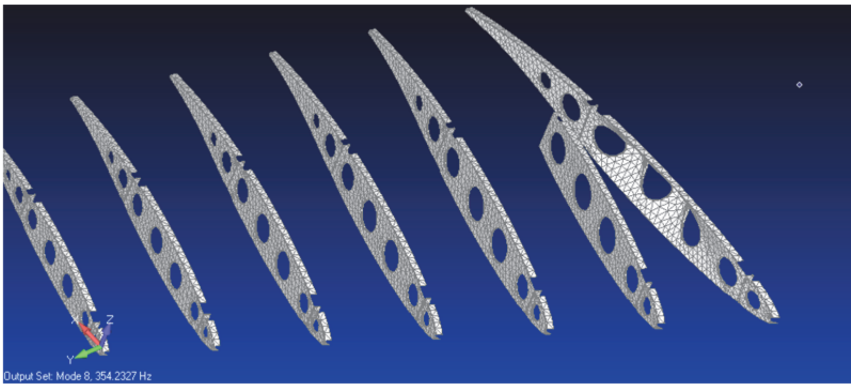

Figure 77 8th mode: 354.2327 Hz

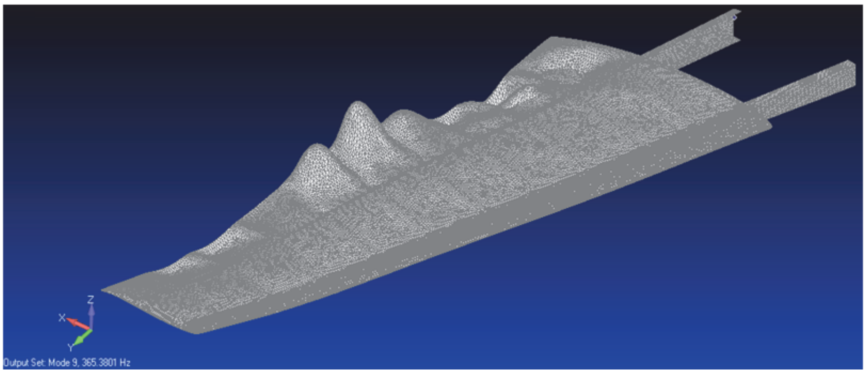

Figure 78 9th mode: 365.3801 Hz

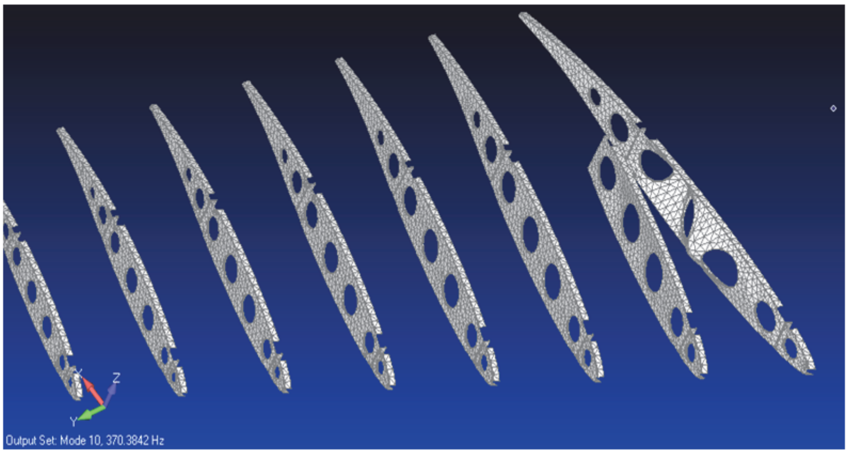

Figure 79 10th mode: 370.3801 Hz

Chapter 6 Conclusions and future works.

In this thesis the design and the optimization of the wind tunnel model of RIBES project has been presented. It has been previously decided to model the geometry with plate elements, so the geometry has been imported in SolidWorks in order to extract mean surfaces.

How to connect the various elements was chosen comparing results and complexity of different connecting methodologies. FEMAP's *Connect, Surfaces* command was found to be the most performing one. The model has been bounded and loaded to represent the testing conditions in the wind tunnel. Load transfer error was check and it was found to be negligible. The model was then validated using the beam and thin plate theories.

A first static analysis was performed to have a baseline on which base further analysis. FEMAP's Sol200 was performed and its results were not satisfying buckling analysis.

A DOE campaign was set, confronting the results of 19 different Design Points so to have a full comprehension of the problem and effect of changing parameters. By means of the DOE campaign results, an optimum set of thicknesses was found, so that static and buckling safeties are both assured.

Next step in order to have the model built is to choose the aluminum alloy with which the model has to be made and to build it so to be ready for wing tunnel tests.

Bibliography

[1] T. Sawada, T. Hisada; *Fluid-structure interaction analysis of the two-dimensional flag-in-wind problem by an interface-tracking ALE finite element method.* 2005

[2] A. Albers, D. Emmerich, P. Häußler; *Automated structural optimization of flexible components using MSC.Adams/Flex and MSC.Nastran Sol200.* 2002

[3] A. Masud, M. Bhanabhagvanwala, R. A. Khurram; *An adaptive mesh rezoning scheme for moving boundary flows and fluid-structure interaction*. 2005

[4] R. Jin, W. Chen, T.W. Simpson; *Comparative studies of metamodelling techniques under multiple modeling criteria.* 2001

[5] A. de Boer, M.S. van der Schoot, H.Bijl; *Mesh deformation based on eadial basis function interpolation*. 2007

[6] S. Jakobsson, O. Amoignon; *Mesh deformation using radial basis functions for gradient-based aerodynamic shape optimization.* 2007

[7] S. Chintapalli; *Preliminary structural design optimization of an Aircraft Wing-box.* 2006

[8] M.E. Biancolini, C. Brutti, E. Pezzuti; *Shape optimization for structural design by means of finite elements method.* 2001

[9] J.J.M. Rupkema, L.F.P. Etman, A.J.G. Schoofs; *Use of Design Sensitivity Information in response and kriging metamodels.* 2001

[10] R. Sedaghti, Mostafa S.A. Elsayed; *Multidisciplinary optimization standardization approach fon integration and configurability, MOSAIC project; Task 6: Wing-box structural design optimization.* 2006

[11] C. Imrak, I. Gerdemeli; *The problem of isotropic rectangular plate with four clamped edges.* 2007

[12] M. Batista; *Uniformly loaded rectangular thin plates with symmetrical boundary conditions*. 2010

[13] E. Ventsel, T. Krauthammer; *Thin plates and shells. Theory, analysis and applications.*

[14] S. Timoshenko, S. Woinowsky-Krieger. *Theory of plates and shells.*

[15] http://simulatemore.mscsoftware.com/

[16] https://www.efunda.com/